The Astrophysical Journal, 833:178 (23pp), 2016 December 20 doi:10.3847/1538-4357/833/2/178

THE GRISM LENS-AMPLIFIED SURVEY FROM SPACE (GLASS). VII. THE DIVERSITY OF THE DISTRIBUTION OF STAR FORMATION IN CLUSTER AND FIELD GALAXIES AT $0.3 \leqslant z \leqslant 0.7$

Benedetta Vulcani[1], Tommaso Treu[2], Kasper B. Schmidt[3], Takahiro Morishita[2,4,5], Alan Dressler[6], Bianca M. Poggianti[7], Louis Abramson[2], Marusa Bradač[8], Gabriel B. Brammer[9], Austin Hoag[8], Matthew Malkan[2], Laura Pentericci[10], and Michele Trenti[1]
[1] School of Physics, University of Melbourne, VIC 3010, Australia
[2] Department of Physics and Astronomy, University of California, Los Angeles, CA, 90095-1547, USA
[3] Leibniz-Institut fr Astrophysik Potsdam (AIP), An der Sternwarte 16, 14482 Potsdam, Germany
[4] Astronomical Institute, Tohoku University, Aramaki, Aoba, Sendai 980-8578, Japan
[5] Institute for International Advanced Research and Education, Tohoku University, Aramaki, Aoba, Sendai 980-8578, Japan
[6] The Observatories of the Carnegie Institution for Science, 813 Santa Barbara St., Pasadena, CA 91101, USA
[7] INAF-Astronomical Observatory of Padova, Italy
[8] Department of Physics, University of California, Davis, CA, 95616, USA
[9] Space Telescope Science Institute, 3700 San Martin Drive, Baltimore, MD, 21218, USA
[10] INAF—Osservatorio Astronomico di Roma Via Frascati 33-00040 Monte Porzio Catone, Italy
Received 2016 August 28; revised 2016 October 7; accepted 2016 October 13; published 2016 December 16

ABSTRACT

Exploiting the slitless spectroscopy taken as part of the Grism Lens-Amplified Survey from Space (GLASS), we present an extended analysis of the spatial distribution of star formation in 76 galaxies in 10 clusters at $0.3 < z < 0.7$. We use 85 foreground and background galaxies in the same redshift range as a field sample. The samples are well matched in stellar mass (10^8–10^{11} $M_\odot$) and star formation rate (0.5–50 $M_\odot$ yr^{-1}). We visually classify galaxies in terms of broad band morphology, Hα morphology, and likely physical process acting on the galaxy. Most Hα emitters have a spiral morphology (41% ± 8% in clusters, 51% ± 8% in the field), followed by mergers/interactions (28% ± 8%, 31% ± 7%, respectively) and early-type galaxies (remarkably as high as 29% ± 8% in clusters and 15% ± 6% in the field). A diversity of Hα morphologies is detected, suggesting a diversity of physical processes. In clusters, 30% ± 8% of the galaxies present a regular morphology, mostly consistent with star formation diffused uniformly across the stellar population (mostly in the disk component, when present). The second most common morphology (28% ± 8%) is asymmetric/jellyfish, consistent with ram-pressure stripping or other non-gravitational processes in 18% ± 8% of the cases. Ram-pressure stripping appears significantly less prominent in the field (2% ± 2%), where the most common morphology/mechanism appears to be consistent with minor gas-rich mergers or clump accretion. This work demonstrates that while environment-specific mechanisms affect galaxy evolution at this redshift, they are diverse and their effects are subtle. A full understanding of this complexity requires larger samples and detailed and spatially resolved physical models.

Key words: galaxies: clusters: general – galaxies: evolution – galaxies: formation – galaxies: general – galaxies: star formation

Supporting material: machine-readable tables

1. INTRODUCTION

Over the last four decades, several studies have shown that galaxy properties correlate with their environment, and these correlations vary as a function of redshfit (e.g., Dressler 1980; Butcher & Oemler 1984; Dressler et al. 1997; Ellis et al. 1997; Poggianti et al. 1999; Lewis et al. 2002; Gómez et al. 2003; Goto et al. 2003; Treu et al. 2003; Kauffmann et al. 2004; Postman et al. 2005; Grützbauch et al. 2011). The discovery of these correlations raised a fundamental question that remains central to this date: how much is galaxy evolution driven by internal processes as opposed to collective phenomena found only in specific environments? This question has sometimes been phrased in terms of nature versus nurture, even though the distinction is not clear-cut: today's clusters correspond to some of the most overdense regions in the early universe and therefore we expect their evolution to be accelerated with respect to average or underdense region, even if cluster-specific mechanisms were not at all relevant (Dressler 1980; Abramson et al. 2016; Lilly & Carollo 2016; Morishita et al. 2016). Thus, one of the key challenges consists of finding observational signatures that uniquely point to a cluster-specific mechanism and then characterizing their overall importance.

For example, the fraction of star-forming galaxies has been found to significantly decrease, going from the dense cluster centers to the field. In clusters at $0 < z < 0.1$ the star formation rate (SFR) in star-forming galaxies also declines with decreasing radius (von der Linden et al. 2010; Paccagnella et al. 2016), as would be expected if cluster-specific environmental processes act to impede star formation. However, there is no consensus between the relative importance of the specific mechanisms at play. It is not even clear whether star formation is actively quenched by the cluster environment or whether it occurs prior to the galaxy entering the cluster sphere of influence. For example, Lewis et al. (2002) found that the fraction of star-forming galaxies strongly decreases with declining radius, but the same correlation holds for galaxies more than two virial radii from the cluster center. They concluded that this rules out cluster-specific processes being solely responsible for the declining fraction of star-forming galaxies toward smaller radii. However, for example, Haines et al. (2013) at $z < 0.15$, and Patel et al. (2009), Vulcani et al.

(2010), and Koyama et al. (2013) at $0.4 < z < 0.8$, and Muzzin et al. (2012) at $0.85 < z < 1.20$ found that within the virial radius the SFRs of star-forming galaxies are significantly lower than those found in field regions, at any given mass. In contrast, for example, Sobral et al. (2011) found that at $z \sim 0.8$ differences hold only at low masses (Koyama et al. 2013); Darvish et al. (2016) showed a lack of environmental dependence of the SFR–mass relation out to $z \sim 1$–2.

Haines et al. (2013) also found that the SFRs of the galaxies in the infall regions are indistinguishable from those in the field. They argue that the processes that suppress the star formation within infalling galaxies must be related to processes occurring within the cluster, likely due to interactions with the intra-cluster medium (ICM).

Muzzin et al. (2012) also argue that the lack of strong correlation of the properties of star-forming and quiescent galaxies with their environment can be understood if the environmental-quenching timescale is rapid, and that the evolution of the internal-quenching and environmental-quenching rates mirrors each other, regardless of which processes dominate the overall quenching process.

We note that while many studies have so far been mostly confined to field versus clusters, intermediate environments such as galaxy groups, outskirts of clusters, and filaments are equally important to shed light on the processes inducing galaxy transformations (e.g., see Kodama et al. 2001; Porter & Raychaudhury 2007; Porter et al. 2008; Sobral et al. 2011; Coppin et al. 2012; Darvish et al. 2014).

The picture is further complicated by the diversity of physical processes that might transform the morphology and star formation properties of galaxies. Internal feedback, likely driven by either supernovae or active galactic nucleus (AGN), and/or low escape velocities might be the responsible for outflows from both star formation and AGN activity to be much more efficient and induce faster transformations (see, e.g., McGee et al. 2014; Sobral et al. 2015). At the same time, many external physical mechanisms can take place. Gravitational effects can distort a galaxy and tear away stars and gas (Bekki 1999). Rapid and frequent galaxy–galaxy encounters induce gravitational perturbations, which can greatly affect the stellar and gas components of cluster galaxies (Moore et al. 1996). Gas falling onto a cluster is heated by shocks leading to a hot, diffuse ICM that permeates the space between the galaxies in clusters. In turn, the ICM can impact the gas within a galaxy by either compressing it, leading to triggered star formation (Bekki & Couch 2003; Stroe et al. 2014, 2015), or by removing the galaxy gas, which is required to fuel star formation and thus quenching star formation. The high-speed relative motion between the galaxy and ICM can induce ram-pressure stripping (Gunn & Gott 1972).

Although all these process are observed to be at work at some level, a number of studies have shown that their overall effects are subtle. Controlling for a galaxy stellar mass and color, environmental differences are small and difficult to detect even in the best spatially unresolved data (Morishita et al. 2016).

Spatially resolved data, preferably spectroscopic, is necessary to make progress, since each process is expected to leave some signature on the spatial distribution of star formation within a galaxy. Broadly speaking, ram pressure is expected to partially or completely strip layers of gas from a galaxy, leaving a recognizable pattern of star formation with truncated disks smaller than the undisturbed stellar disk (e.g., Yagi et al. 2015). The morphology of the gas should also reflect the motion of the galaxy through the ICM. Strangulation, which is the removal of the hot gas halo surrounding the galaxy either via hydrodynamical or tidal effects (Larson et al. 1980; Balogh et al. 2000), should deprive the galaxy of its outer gas reservoir but have a much gentler effect on the deeply embedded interstellar medium (ISM) and diffuse star formation. Wet major and minor mergers, cold gas accretion, and harassment should also leave relatively significant signatures in the gas dynamics (Moore et al. 1996).

Recent progress in hydrodynamical numerical simulations (e.g., FIRE, Hopkins et al. 2014) that are starting to resolve individual star-forming regions within galaxies suggests that in the near future it will be possible to go beyond these qualitative statements to full quantitive characterizations of the signatures of these processes.

The most commonly adopted tracer of instantaneous star formation is the Hα line emission as it scales with the quantity of ionizing photons produced by hot young stars (Kennicutt 1998). In the local universe, a number of studies have focused on the analysis of the Hα spatial distribution of a limited number of systems in clusters clearly presenting signs of stripping (e.g., Merluzzi et al. 2013, 2016; Fumagalli et al. 2014; Fossati et al. 2016; B. M. Poggianti et al. 2016, in preparation).

While several spatially resolved studies of Hα have been conducted beyond the local universe from the ground (e.g., Yang et al. 2008; Gonçalves et al. 2010; Swinbank et al. 2012; Bretherton et al. 2013; Sobral et al. 2013; Wisnioski et al. 2015; Stott et al. 2016), very few studies have been conducted at $z = 0$–1 from space (e.g., Atek et al. 2010; Straughn et al. 2011; Livermore et al. 2012). Spatially resolved star formation maps at $z \sim 1$ have been obtained for field galaxies using both the Advanced Camera for Surveys (ACS) I band and the G141 grism on the Wide-Field Camera 3 (WFC3) on board the *Hubble Space Telescope* (*HST*) as part of the 3D-*HST* Survey (van Dokkum et al. 2011; Brammer et al. 2012; Schmidt et al. 2013; Momcheva et al. 2015). Nelson et al. (2012, 2013, 2015) mapped the Hα and stellar continuum with high resolution, showing that star formation broadly follows the rest-frame optical light, but is slightly more extended. By stacking galaxies in bins of stellar mass, they found that star formation has to occur in approximately exponential distributions on average and is enhanced at all radii above the star formation main sequence (SFMS, Noeske et al. 2007) and suppressed at all radii below the SFMS.

Wuyts et al. (2012, 2013) characterized the resolved stellar populations with multi-wavelength broad band imaging from CANDELS (Grogin et al. 2011; Koekemoer et al. 2011) and Hα surface brightness profiles from 3D-*HST* (Brammer et al. 2012) at $z = 0.7$–1.5 at the same kiloparsec resolution. They found that Hα morphologies resemble more closely those observed in the ACS F814W band than in the WFC3/F160W band, especially for the larger systems. In addition, they showed how the rate of ongoing star formation per unit area tracks the amount of stellar mass assembled over the same area. Off-center clumps are characterized by enhanced Hα equivalent widths, bluer broad band colors, and correspondingly higher specific SFRs than the underlying disk, suggesting that the ACS clump selection preferentially picks up those regions of elevated star formation activity that are the least obscured by dust.

Table 1
Cluster Properties

Cluster	Short name	R.A. (J2000)	Decl. (J2000)	z	Phys Scale (kpc/″)	L_X (10^{44}erg s^{-1})	M_{500} ($10^{14}M_\odot$)	r_{500} (Mpc)	PA1	PA2
Abell2744	A2744	00:14:21.2	−30:23:50.1	0.308	4.535	15.28 ± 0.39	17.6 ± 2.3	1.65 ± 0.07	135	233
RXJ2248.7-4431	RXJ2248	22:48:44.4	−44:31:48.5	0.348	4.921	30.81 ± 1.57	22.5 ± 3.3	1.76 ± 0.08	053	133
Abell370	A370	02:39:52.9	−01:34:36.5	0.375	5.162	8.56 ± 0.37	11.7 ± 2.1	1.40 ± 0.08	155	253
MACS0416.1-2403	MACS0416	04:16:08.9	−24:04:28.7	0.420	5.532	8.11 ± 0.50	9.1 ± 2.0	1.27 ± 0.09	164	247
RXJ1347.5-1145	RXJ1347	13:47:30.6	−11:45:10.0	0.451	5.766	47.33 ± 1.2	21.7 ± 3.0	1.67 ± 0.07	203	283
MACS1423.8+2404	MACS1423	14:23:47.8	+24:04:40	0.543	6.382	13.96 ± 0.52	6.64 ± 0.88	1.09 ± 0.05	008	088
MACS1149.6+2223	MACS1149	11:49:36.3	+22:23:58.1	0.544	6.376	17.25 ± 0.68	18.7 ± 3.0	1.53 ± 0.08	032	125
MACS0717.5+3745	MACS0717	07:17:31.6	+37:45:18	0.546	6.400	24.99 ± 0.92	24.9 ± 2.7	1.69 ± 0.06	020	280
MACS2129.4-0741	MACS2129	21:29:26.0	−07:41:28.0	0.589	6.524	13.69 ± 0.57	10.6 ± 1.4	1.26 ± 0.05	050	328
MACS0744.9+3927	MACS0744	07:44:52.8	+39:27:24.0	0.686	7.087	18.94 ± 0.61	12.5 ± 1.6	1.27 ± 0.05	019	104

Note. J2000 coordinates, redshift, physical scale, X-ray luminosity, M_{500} (from Mantz et al. 2010), r_{500}, and the two position angles.
(This table is available in machine-readable form.)

In this paper, we exploit the unprecedented depth and angular resolution of WFC3 G102 grism data set obtained as part of the Grism Lens-Amplified Survey from Space (GLASS; GO-13459; PI: Treu,[11] Schmidt et al. 2014; Treu et al. 2015) to carry out a large and detailed study of the Hα morphology in clusters and field galaxies at $0.3 < z < 0.7$. Building on the techniques developed in our pilot study (Vulcani et al. 2015), we increase the sample size from 25 and 17 to 76 and 85 galaxies in the clusters and the field, respectively. We define and apply a new morphological classification scheme for Hα emission to this full statistical sample with the goal of identifying potential signatures of the underlying physical processes and assess their frequency across environments, and across the SFR–mass plane.

In a companion paper (Vulcani et al. 2016; hereafter Paper VIII), we investigate trends with cluster properties, such as the hot gas density as traced by the X-ray emission, the total surface mass density as inferred from gravitational lens models, and the local number density, to inspect whether or not local cluster conditions have an impact on the extent and location of the star formation.

The paper is structured as follows. Section 2 introduces the data set, along with the data reduction and the redshift determinations. Section 3 describes the sample and how galaxy properties have been determined. Section 4 presents our results, mainly focussing on the morphology of Hα emitters at different wavelengths and on the physical processes that are likely to have induced these morphologies. We also quantify the position and extension of the Hα emission within the galaxies and characterize the SFR–mass relation for the different types of Hα emitters. Focusing on spirals, we test the hypothesis that star formation is mainly occurring in the disk. In Section 5 we discuss our results and conclude.

Throughout the paper, we assume $H_0 = 70$ km s^{-1} Mpc^{-1}, $\Omega_0 = 0.3$, and $\Omega_\Lambda = 0.7$. The adopted initial mass function (IMF) is that of Chabrier (2003) in the mass range 0.1–100 $M_\odot$.

2. THE GRISM LENS-AMPLIFIED SURVEY FROM SPACE DATA SET

GLASS is a 140 orbit slitless spectroscopic survey conducted with *HST* in cycle 21. It has observed the cores of 10 massive galaxy clusters with the WFC3 NIR grisms G102 and G141 providing an uninterrupted wavelength coverage from 0.8μm to 1.7μm. The 10 clusters are listed in Table 1. Observations for GLASS were completed in 2015 January, and the first public data release was completed in 2016 March. Prior to each grism exposure, imaging through either F105W or F140W was obtained to assist the extraction of the spectra and the modeling of contamination from nearby objects on the sky. The total exposure time per cluster was 10 orbits in G102 (with either F105W or F140W) and 4 orbits in G141 with F140W. Each cluster was observed at two position angles (PAs) approximately 90 degrees apart to facilitate clean extraction of the spectra for objects in crowded cluster fields. Six GLASS clusters are imaged by the Hubble Frontier Fields (HFF; P.I. Lotz, Lotz et al. 2016) and eight by the Cluster Lensing And Supernova survey with Hubble (CLASH; P.I. Postman, Postman et al. 2012), providing excellent multiband data.

2.1. Data Reduction

The GLASS observations follow the updated version of the 3D-*HST* reduction pipeline[12] described by Brammer et al. (2012), Momcheva et al. (2015). The updated pipeline combines the individual exposures into mosaics by interlacing them.

Each exposure was interlaced to a final G102 (G141) grism mosaic. Before sky-subtraction and interlacing, each individual exposure was checked and corrected for elevated backgrounds due to the He Earth-glow described by Brammer et al. (2014). From the final mosaics, the spectra of individual objects are extracted by predicting the position and extent of each two-dimensional spectrum based on the SExtractor (Bertin & Arnouts 1996) segmentation map combined with a deep mosaic of the direct NIR GLASS and CLASH images. As this is done for each object, the contamination, i.e., the dispersed light from neighboring objects in the direct image field of view, can be estimated and accounted for. Full details on the observations and data reduction are given in Treu et al. (2015), while a complete description of the 3D-*HST* pipeline, spectral extractions, and spectral fitting, is provided by Momcheva et al. (2015).

The spectra analyzed in this study were all visually inspected with the publicly available GLASS inspection GUI, GiG[13]

[11] http://glass.astro.ucla.edu

[12] http://code.google.com/p/threedhst/

[13] https://github.com/kasperschmidt/GLASSinspectionGUIs

(Treu et al. 2015), to identify and flag systematic errors in the contamination model, assess the degree of contamination in the spectra, and identify strong emission lines and the presence of a continuum.

2.2. Redshift Determinations

To determine redshifts, templates were compared to each of the four available grism spectra independently (G102 and G141 at two PAs each) to compute a posterior distribution function for the redshift. If available, photometric redshift distributions were used as input priors to the grism fits to reduce computational time. Then, with the help of the publicly available GLASS inspection GUI for redshifts (GiGz, Treu et al. 2015), we flagged which grism fits are reliable or alternatively entered a redshift by hand if the redshift was misidentified by the automatic procedure. Using GiGz we assigned a quality Q_z to the redshift (4 = secure; 3 = probable; 2 = possible; 1 = tentative, but likely an artifact; 0 = no-z). These quality criteria take into account the signal-to-noise ratio of the detection, the possibility that the line is a contaminant, and the identification of the feature with a specific emission line. This procedure was carried out independently by at least two inspectors per cluster (see Treu et al. 2015, for details).

The full redshift catalogs from the inspection of the 10 GLASS clusters are available online (https://archive.stsci.edu/doi/resolve/resolve.html?doi=10.17909/T9KG60).

3. THE SAMPLE

We make use of all the 10 GLASS clusters. Virial radii r_{500} have been computed from virial masses M_{500} taken from Mantz et al. (2010):

$$r_{500} = \sqrt[3]{\frac{3}{4\pi}\frac{M_{500}}{500\rho_{cr}}}$$

where $\rho_{cr} = \frac{3H^2}{8\pi G} = \frac{3H_0^2}{8\pi G} \times [\Omega_\Lambda + \Omega_0 \times (1+z)^3)]$, with G being the gravitational constant $= 4.29 \times 10^{-9}(\mathrm{km/s})^2$ Mpc $M_\odot$.

From the redshift catalogs, we extract galaxies with reliable redshift ($Q_z \geqslant 2.5$) within ± 0.03 of the cluster redshift and consider them as cluster members. The redshift uncertainty is larger than the expected range of cluster velocities in order to account for uncertainties in the low-resolution grism data. Our sample members might therefore include a fraction of interlopers, but we expect it to be extremely small, considering that we are looking at the cores of rich clusters that are highly overdense (see, e.g., Morishita et al. 2016).

We then select galaxies with detected Hα emission. We exclude the Brightest Cluster Galaxies (BCGs) from our analysis, which are not representative of the general cluster galaxy population. Given the cluster redshifts, Hα is found at the observed wavelength range $8500 \leqslant \lambda \leqslant 11100$ Å, and we therefore mostly exploit the G102 grism data in our analysis, but we check whether Hα is detected in the G141 grism for the higher redshift galaxies ($z \geqslant 0.67$, i.e., members of MACS0744 and a few field galaxies).

We assemble a field sample consisting of all galaxies with reliable redshift, Hα in emission in the G102 grism and redshift outside the cluster redshift intervals ($z < z_{\rm cl} - 0.03$ or $z > z_{\rm cl} + 0.03$). Overall, we limit our field sample range to the redshift range spanned by cluster members: $0.3 \leqslant z \leqslant 0.7$. Note that this cut was not adopted by Vulcani et al. (2015), and therefore some galaxies from that work are not included in the current selection. Figure 1 shows the redshift distribution of our samples. We do not have additional information on the environments of the field galaxies; some of them might actually be located in groups, but certainly not in rich clusters.

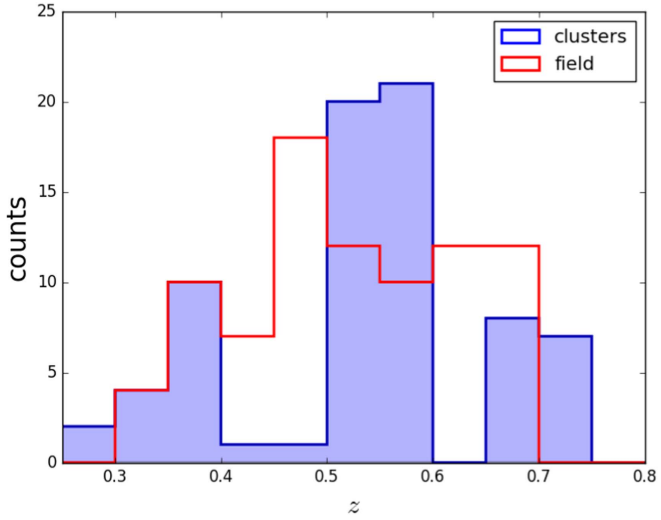

Figure 1. Redshift distribution for cluster (blue) and field (red) galaxies in our sample.

Table 2
Number of Galaxies with Hα in Emission

Cluster	Cluster Members	Field Galaxies
A2744	4	5
RXJ2248	3	4
A370	8	10
MACS0416	2	5
RXJ1347	2	8
MACS1423	10	18
MACS1149	8	7
MACS0717	16	8
MACS2129	8	12
MACS0744	15	8
total	76	85

Overall, our sample includes 76 cluster members and 85 field galaxies, distributed among the different clusters as summarized in Table 2.

3.1. Stellar Masses

Stellar mass estimates are obtained as described by Morishita et al. (2016). Seven *HST*/WFC3+ACS bands (F435W, F606W, F814W, F105W, F125W, F140W, and F160W) have been used. Briefly, the SED parameters for all galaxies have been derived using FAST v.1.0 (Kriek et al. 2009) using the spectroscopic redshift of each object. CLASH (Postman et al. 2012) or, when available, HFF photometry (Lotz et al. 2016) has been adopted. The stellar population model of GALAXEV (Bruzual & Charlot 2003), solar metallicity, and a Chabrier (2003) IMF have been adopted. The Calzetti dust law (Calzetti et al. 2000) is restricted to the range $0 \leqslant A_V \leqslant 4.0$ mag and the age can vary from 0.1 to the age of the universe at the galaxy redshift. Exponentially declining star formation history, where $\mathrm{SFR}(t) \propto \exp(-t/\tau)$ at the time t, with τ in the range of

$8 \leqslant \log\tau \leqslant 10$ is assumed. The errors in the SED parameters are 1σ uncertainties derived by FAST.

We note that the templates for SED fitting used here do not include emission lines. In Vulcani et al. (2015), where we analyzed only two clusters, we had used an SED fitting procedure that considered emission lines (see Castellano et al. 2014, for details). Comparing those mass estimates to the one used here for the subset of objects in common, after correcting for the IMF, we get that results are largely in agreement and the dispersion is <0.1dex, which is smaller than the typical error on mass estimates (0.2–0.3 dex).

Stellar population properties have not been fitted for A370, since the final HFF observations are not scheduled until 2016 September.

3.2. Hα Maps

The GLASS grism spectra have high spatial resolution and low spectral resolution, meaning that emission line structure reflects almost exclusively spatial structure (morphology) in contrast to data with high spectral resolution where structure reflects velocity (rotation or dispersion). Spectra can be seen as images of a galaxy taken at ∼24 Å increments (∼12 Å after interlacing) and placed next to each other (offset by one pixel) on the detector.

The details of the procedure we followed to make emission line maps of galaxies are described by Vulcani et al. (2015). Briefly, we obtained the maps from the spectra coming from the different exposures (one per PA) of each galaxy independently, and only in the last step we combined them. From the flux-calibrated galaxy two-dimensional (2D) continuum spectra we subtracted the sky background and the contamination. From two regions contiguous to the Hα emission we determined the *y*-position of the peak of the continuum. This position was needed to measure the offset in the *y*-direction of the Hα emission with respect to the galaxy center in the light of the continuum. Subsequently, we subtracted the 2D stellar continuum model obtained by convolving the best-fit one-dimensional continuum without emission lines with the actual 2D data, ensuring that all model flux pixels are non-negative. We were therefore left with the surface brightness map of the Hα line.

When spectra from both PAs are reliable, i.e., not contaminated by other sources or not at the edge of the grism, we combined the maps obtained for the two PAs. When also the Hα maps from the G141 filter are available, we combined them with the G102 maps, to increase the signal-to-noise ratio. Overall, for 80 galaxies Hα maps have been reliably obtained in the spectra of both PAs in the G102 grism; for 9 galaxies Hα maps have been obtained also from the G141 spectra.

As a final step, we superimposed the Hα map onto an image of the galaxy taken with the F475W filter (rest-frame UV) and onto an image in the F140W (IR). Images are taken from the HFF photometry (Lotz et al. 2016) or CLASH *HST* photometry, (Postman et al. 2012). We use the F475W filter to map relatively recent (∼100 Myr) star formation, and the F140W to trace the older stellar population as opposed to ongoing (∼10Myr) star formation traced by Hα . Note that for A2744 we used the F435W filter, because the F475W filter is not available.

To superimpose the Hα maps to the images, we aligned each map to the continuum image of the galaxy, rotating them by the angle of its PA, keeping the *y*-offset unaltered with respect to the continuum. On the *x*-axis, there is a degeneracy between the spatial dimension and the wavelength uncertainty; it is therefore not possible to determine uniquely the central position of the Hα map for each PA separately. However, for the vast majority of cases in which spectra from both PAs are reliable, we used the fact that the two PAs differ by almost 90°; therefore the *x*-direction of one spectrum roughly corresponds to the *y*-direction of the second spectrum and vice-versa. We shifted the two spectra independently along their *x*-direction to maximize the cross correlation between the two maps to get the intersect. For the galaxies with reliable spectra in both PAs, we also measured the real distance between the peak of the Hα emission and the continuum emission, obtained as the quadratic sum of the two offsets.

3.3. SFRs

From the Hα maps we derive SFR maps. We use the conversion factor derived by Kennicutt et al. (1994) and Madau et al. (1998):

$$\mathrm{SFR}[M_\odot\ \mathrm{yr}^{-1}] = 5.5 \times 10^{-42} L(\mathrm{H}\alpha)[\mathrm{erg\ s}^{-1}]$$

valid for a Kroupa (2001) IMF. We then converted SFRs to our adopted Chabrier (2003) IMF by adding 0.05 dex to the logarithmic values. We compute both the surface SFR density (ΣSFR, $M_\odot\ \mathrm{yr}^{-1}\,\mathrm{kpc}^{-2}$) and the total SFRs ($M_\odot\ \mathrm{yr}^{-1}$) separately for the spectra coming from the two PAs and then combine them taking the mean values. Errors are summed in quadrature and divided by two. The measurements from the two PAs are consistent within the uncertainty. The total SFRs are obtained, summing the surface SFR density within the Kron radius measured by Sextractor from a combined NIR image of the galaxy.

There are two possible limitations when using Hα as an SFR estimator: the contamination by the [N II] line doublet, and uncertainties in the extinction corrections to be applied to each galaxy. We account for both effects, even though they are both small and none of the conclusions of this work hinge on the details of these corrections.

To correct for the [N II] contamination, we apply the locally calibrated correction factor given by James et al. (2005). As opposed to previous works, which considered only central regions, these authors developed a method that takes into account the variation of the Hα–[N II] with radial distance from the galaxy center, finding an average value of $\mathrm{H}\alpha/(\mathrm{H}\alpha + [\mathrm{N\ II}]) = 0.823$. This approach is appropriate given our goal to investigate extended emission.

The second caveat is the effect of dust extinction. Star formation normally takes place in dense and dusty molecular clouds, so a significant fraction of the emitted light from young stars is absorbed by the dust and re-emitted at rest-frame IR wavelengths. Garn & Best (2010) modeled a mass-dependent attenuation by dust, based on the Calzetti et al. (2000) dust attenuation law, of the form

$$A(\mathrm{H}\alpha) = \sum_{i=0}^{3} B_i \cdot X^i \quad (1)$$

with $X = \log_{10}(M_*/1.1 \cdot 10^{10} M_\odot)$ (to take into account the different IMF) and $B_i = 0.91$, 0.77, 0.11, and −0.09, respectively.

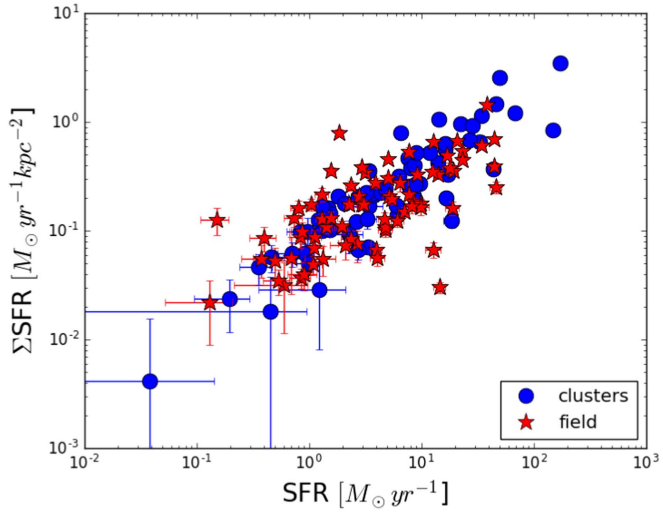

Figure 2. ΣSFR–SFR for cluster (blue) and field (red) galaxies in our sample. Error bars show the typical uncertainties on the measurements. Our ΣSFR limit is around $5 \times 10^{-2}\ M_\odot\ \mathrm{yr}^{-1}\ \mathrm{kpc}^{-2}$ for SFR $\sim 1 M_\odot\ \mathrm{yr}^{-1}$ and is independent on environment, suggesting that the physical conditions in star-forming galaxies are similar in clusters and field.

Even though the relationship was measured from observations of $z \sim 0$ starburst galaxies, it has been shown to be appropriate for galaxies at redshifts up to $z \sim 0.8$ (see, e.g., Garn et al. 2010; Sobral et al. 2012; Domínguez et al. 2013; Price et al. 2014).

According to Garn & Best (2010), the equation allows to predict the extinction of a galaxy with a given stellar mass to within a typical error of 0.28 mag. This typical error is broadly comparable to the accuracy with which extinctions can be estimated from the Balmer decrement. We use this correction to obtain the intrinsic SFRs:

$$\mathrm{SFR}_{\mathrm{int}} = \mathrm{SFR}_{\mathrm{obs}} \times 10^{A(\mathrm{H}\alpha)\times 0.4}.$$

We assume that there is no spatial variation in extinction across the galaxy, even though high-resolution imaging in multiple *HST* bands (Wuyts et al. 2012) and analyses of such data in combination with Hα maps extracted from grism spectroscopy (Wuyts et al. 2013) indicate that such an assumption may be oversimplistic, particularly in the more massive galaxies where the largest spatial color variations are seen. It is hard to anticipate how corrections for non-uniform extinction might affect our conclusions, since the correction to the sizes will depend on the actual distribution of dust.

However, we expect the effect of dust to be relatively small, especially in a differential sense, i.e., it should not effect significantly our comparison between cluster and field galaxies. In support of this we note that Wang et al. (2016) measure dust attenuation from the Balmer decrement for a subsample of field galaxies at $1.3 \leqslant z \leqslant 2.3$ in MACS1149. They find that the measured attenuation A_V is almost always much smaller than 1 mag, and quite homogeneous across the galaxies, indicating that the spatial variation of the dust is not very important.

Figure 2 shows the correlation between ΣSFRs and total SFR. Our ΣSFR limit is around $5 \times 10^{-2}\ M_\odot\ \mathrm{yr}^{-1}\ \mathrm{kpc}^{-2}$ for SFR $\sim 1 M_\odot\ \mathrm{yr}^{-1}$ both in clusters and in the field, suggesting that poor sensitivity does not vary between the field and cluster samples, as expected because we are using the same data set. We use this value as an indication of the completeness limit of our samples.

3.4. Hα EWs

Finally, we also compute Hα equivalent widths EW(Hα) from the collapsed 2D spectra. We define the line profile by adopting a fixed rest-frame wavelength range, centered on the theoretical wavelength, 6480-6650 Å, and then obtain the line flux, f_{line}, by summing the flux within the line. The continuum is defined by two regions of 100 Å located at the two extremes of the line profile. We fit a straight line to the average continuum in the two regions and sum the flux below the line, to obtain f_{cont}. The rest-frame EW(Hα) is therefore defined by

$$\mathrm{EW}(\mathrm{H}\alpha) = \frac{f_{\mathrm{line}}}{f_{\mathrm{cont}} \times (1+z)}$$

Our approach ignores underlying Hα absorption, assuming it to be negligible for these strong emitters. As usual, when two spectra for the same galaxy are reliable, the final value is given by the average of the two EW estimates, and the error is obtained by summing in quadrature the individual errors. Overall, the EW measurements from the two PAs are consistent within the uncertainties.

3.5. Sizes and B/T Ratios

Morphological parameters (sizes, bulge-to-total (B/T) ratios) for all the galaxies have been obtained using GALFIT (Peng et al. 2002), as described by Morishita et al. (2016). Measurements have been performed using the F140W and F375W for HFF photometry (Lotz et al. 2016) or the F140W and F475W for CLASH *HST* photometry (Postman et al. 2012).

The fitting was performed assuming a double profile, to separate the different components of the galaxies (i.e., bulge +disk). Following a common choice (e.g., Graham & Driver 2005; Meert et al. 2015), for bulges a Sérsic index $n = 4$ has been adopted, while for disks the typical exponential profile has been chosen ($n = 1$). Such decomposition allows us to inspect whether or not the Hα flux traces the disk. A detailed description of the fitting procedure—though only for a single component analysis—can be found in Morishita et al. (2016).

To estimate the Hα size of the galaxies, we choose to fix the Sérsic index to $n = 1$. This assumption is valid only for galaxies where star formation is taking place in disks, as we will discuss in Section 4.6. Therefore, we run GALFIT with the same parameters as done for the disk component in the continuum.

3.6. Visual Morphologies

Galaxies in our sample have been visually inspected by a subset of authors (B.V., T.T., A.D., and T.M.) to classify their morphology. Visual inspection was carried out with the publicly available Graphic User Interface GIG for morphologies (GiGm) described in Appendix B. We classified both the broad band morphology and the morphology of the Hα emission. For the former, we followed the standard Hubble classification, subdividing galaxies into Ellipticals (E), Lenticulars (S0), Spirals (Sp), and Irregulars (Irr). In addition, we flagged galaxies undergoing a either minor or major merger

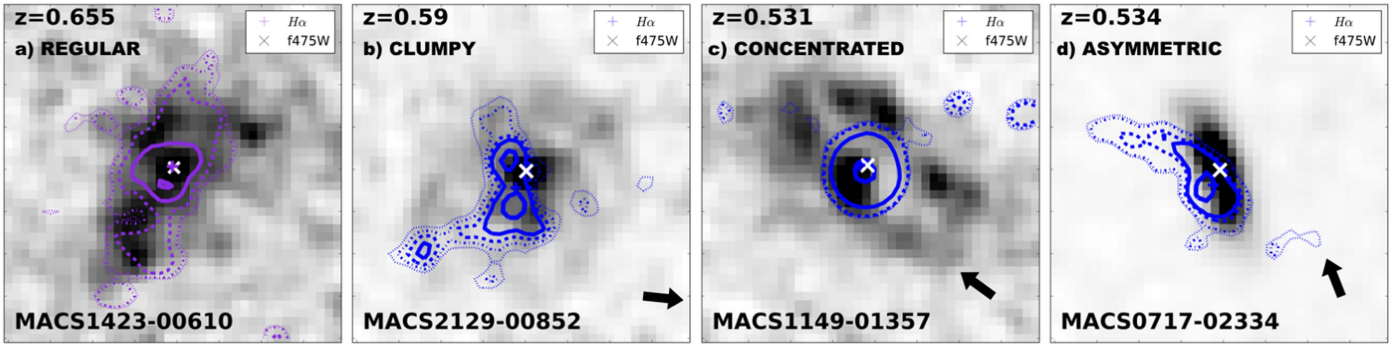

Figure 3. Examples of Hα maps with different morphologies, as indicated in the labels. Maps are superimposed on the image of the galaxy in the F475W filter. Contour levels represent the 35th, 50th, 65th, 80th, and 95th percentiles of the light distribution, respectively. Blue contours indicate that the Hα map is obtained just from one spectrum; purple contours indicate that the Hα map is obtained from the two orthogonal spectra. For galaxies in clusters, arrows in the bottom right corner indicate the direction of the cluster center. The redshift of the galaxy is indicated in the top left corner.

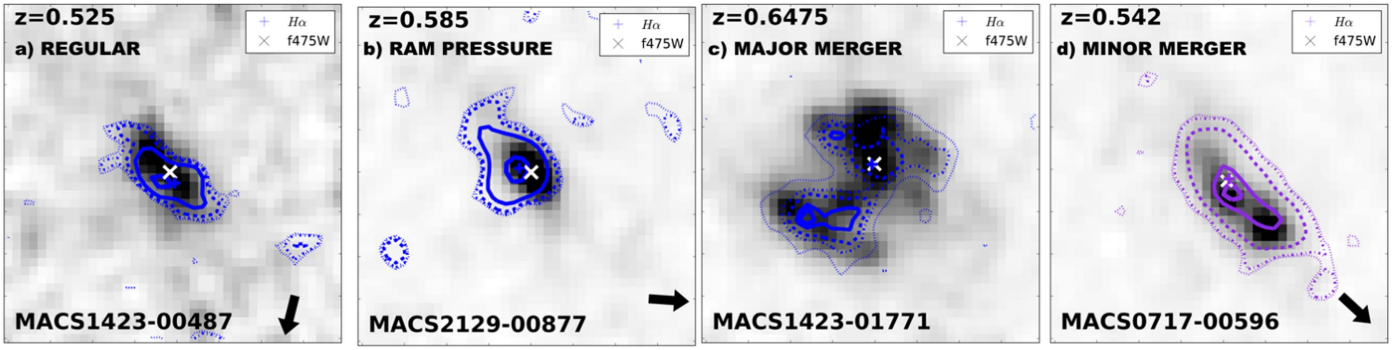

Figure 4. Examples of Hα maps influenced by different physical processes, as indicated in the labels. Colors, lines, and symbols are as in Figure 3.

(Mer). For the Hα morphology, we introduce a new scheme (illustrated in Figure 3):

1. *Regular*, when the Hα light distribution is smooth and follows the galaxy disk (Figure 3(a)).
2. *Clumpy*, when multiple peaks in the Hα light distribution have been detected, possibly a consequence of a merger where the core of the two galaxies are still distinguishable (Figure 3(b)).
3. *Concentrated*, when the Hα light distribution appears more concentrated than the underlying disk or overall continuum if a disk is no clearly identifiable (Figure 3(c)).
4. *Asymmetric/jellyfish*, when the emission appears torqued and extends mainly on one side of the galaxy (Figure 3(d)).

In addition, we also assign a label to each galaxy to attempt to classify the most likely physical processes responsible for altering its continuum and Hα morphology. This is clearly a qualitative and approximate classification scheme, considering that multiple processes might be simultaneously at work and that the mapping between morphology and process is not always unique and unambiguous. In spite of the uncertainties, we believe there is merit in categorizing in a self-consistent manner the diversity of morphological features across environments. In the future, this classification scheme might be replaced with full 2D comparisons with numerical simulations. However, this is not currently possible and a qualitative classification appears to be a useful first step.

We adopt the following scheme (illustrated in Figure 4):

1. *Regular*, when the Hα light distribution appears regular and undisturbed (Figure 4(a)).
2. *Ram pressure*, when an asymmetry in the Hα distribution or in the surface brightness is detected (Figure 4(b)). We are not able to detect weak cases of ram-pressure stripping, for example when a galaxy is at its second or third passage toward the galaxy center, but only the strongest ones, when large quantities of gas are still available, and the ionized gas is stripped away in a line that approximately points away from the cluster center. Even though we know the environment in which galaxies are embedded, in clusters we did not explicitly use the direction of the cluster center to characterize this process. Appendix A shows all the galaxies in our sample that we think are mainly affected by this process.
3. *Major merger*, when the constituents of the mergers are both visible both in the F140W and F475W filters, suggesting they have comparable stellar mass and luminosity (Figure 4(c)).
4. *Minor merger/interaction*, when the F475W filter shows the presence of material infalling onto the main galaxies that is not detected in the F140W filter, suggesting a low mass-to-light ratio and a low stellar mass (Figure 4(d)).
5. *Other*, when none of the above applies.

To determine whether or not our Hα emitters are characterized by a distinctive morphology with respect to the general

Table 3
Properties of Galaxies

Objname	R.A. (J2000)	Decl. (J2000)	z[a]	env	MAG_AUTO ABmag	$\log M_*/M_\odot$	EW Å	SFR ($M_\odot$ yr^{-1})	ΣSFR ($M_\odot$ yr^{-1} kpc^2)	OffsetPA1[b] (kpc)	OffsetPA2[b] (kpc)	Morph[c]	Hα morph[d]	proc Hα [e]
A2744-00065	3.57700058	−30.37947795	0.496	field	20.4	10.3	30.7 ± 0.6	2.7 ± 0.9	0.08 ± 0.03	⋯	−0.1 ± 0.1	Ell	Reg	RP
A370-00765	39.95471146	−1.55565658	0.576	field	21.0	⋯	39 ± 2	⋯	⋯	0.1 ± 0.2	⋯	Mer	Cl	MaM
MACS0416-00286	64.032599	−24.063501	0.312	field	22.4	8.7	70 ± 20	1.3 ± 0.4	0.05 ± 0.01	0.2 ± 0.6	⋯	Unc	Cl	MiM
MACS0717-00173	109.39848457	37.766442326	0.556	cluster	22.1	9.3	30 ± 2	3.7 ± 0.3	0.22 ± 0.01	⋯	−0.0 ± 0.1	S0	Asy	MiM
MACS0744-00175	116.22258717	39.47348495	0.488	field	21.7	9.3	54 ± 4	4.9 ± 0.7	0.11 ± 0.01	−0.9 ± 0.2	0.0 ± 0.2	Spir	Conc	Reg
MACS1149-00063	177.397721	22.415211	0.536	cluster	21.8	9.9	9.7 ± 0.5	4.5 ± 0.7	0.18 ± 0.03	0.0 ± 0.2	⋯	S0	Conc	RP
MACS1423-01729	215.94220899	24.0667282	0.460	field	22.6	8.9	42 ± 4	1.6 ± 0.2	0.13 ± 0.02	0.0 ± 0.1	−0.8 ± 0.2	Spir	Asy	MiM
MACS2129-00163	322.35546305	−7.67532645	0.466	field	21.4	9.6	15.2 ± 0.4	4.0 ± 0.4	0.28 ± 0.03	⋯	−0.2 ± 0.1	Spir	Conc	Reg
RXJ1347-01406	206.89375736	−11.76375986	0.538	field	21.4	9.6	65 ± 2	13.2 ± 0.6	0.67 ± 0.03	0.08 ± 0.04	0.49 ± 0.04	Mer	Ass	MaM
RXJ2248-00104	342.16731251	−44.51393496	0.343	cluster	19.7	9.9	17.4 ± 0.5	28 ± 2	0.70 ± 0.04	1.1 ± 0.1	−0.3 ± 0.2	Spir	Ass	RP

Notes. J2000 coordinates, redshift, environment, magnitude, stellar mass, Hα equivalent width, SFR, ΣSFR, offsets between the Hα emission and the continuum emission (as measured form the F475W filter) along the two directions, broad band continuum morphologies, Hα morphologies, and main processes acting on the galaxy (see text for details). The whole table is available in the online journal.

[a] redshifts slightly changed from the GLASS catalog to better match the center of the Hα maps.

[b] Reported offsets are along the y-direction of the corresponding PA. The orientation of the offset (counterclockwise from North) is $\theta = -\mathrm{PA1} - 44.69$.

[c] Ell = elliptical, S0 = lenticular, Spir = spiral, Irr = Irregular, Mer = merger.

[d] Reg = regular, Cl = Clumpy, Conc = concentrated, Asy = asymmetric/jellyfish.

[e] Reg = nothing, RP = ram-pressure stripping, MaM = Major Merger, MiM = Major Merger, other = other.

(This table is available in its entirety in machine-readable form.)

galaxy population, we also visually classified a control sample of non-Hα emitter galaxies. This sample was drawn from the GLASS subsample for which photometric redshifts have been determined by Morishita et al. (2016). This sample includes four HFF clusters: A2744, MACS0416, MACS0717, and MACS1149. For each galaxy in our Hα emitter sample, we extracted two galaxies from the photo$-z$ sample with masses similar to the reference galaxy (usually one slightly less massive and one slightly more massive), in the same environment and possibly at similar redshift. The latter criterion had to be relaxed for cluster galaxies at $z > 0.55$ due to the lack of cluster galaxies in this redshift range in the photo$-z$ catalog.

The classifications obtained from the different inspectors have been combined, adopting the most common classification. In case of broad disagreement (<25% of the cases), the galaxies were re-inspected and discussed to reach an agreement.

3.7. Summary of the Samples

In summary we have four galaxy sub-samples with the following quantities estimated that we will use in our analysis.

1. Hα emitters, clusters: Continuum morphology, Hα morphology, main process, SFR, ΣSFR, M_*, offsets between emissions, and sizes.
2. Hα emitters, field: Continuum morphology, Hα morphology, main process, SFR, ΣSFR, M_*, offsets between emissions, and sizes.
3. Non-Hα emitters clusters: Continuum morphology and M_*.
4. Non-Hα emitters field: Continuum morphology and M_*.

The first two samples constitute the main sample, the others are our control sample. In the next section we present extensive comparisons of these four samples and their derived characteristics.

4. RESULTS

The properties of galaxies in our main sample are given in Table 3 (the total sample is given in the online journal). They include galaxy positions, redshifts, environments, magnitudes, stellar masses, EW(Hα)s, SFRs, ΣSFRs, the offset between the peak of the light in Hα and in the rest-frame UV continuum, broad band morphologies and Hα morphologies, and main processes acting on the galaxies.

Figure 5 shows the distribution of stellar masses for our main sample. Galaxies in the two environments are characterized by very similar mass distributions (in agreement with Vulcani et al. 2013). Therefore, any differences in star formation properties are not driven by differences in stellar mass.

In the next subsections we will use all the data at our disposal to investigate a number of aspects related to galaxy evolution in the different environments. We will first focus on the morphologies of our galaxies and contrast the morphological distribution of Hα emitters to that of the control sample of non-Hα emitters. Then we will focus only on Hα emitters and consider also the morphology of the Hα emission and characterize the possible processes responsible for such morphologies in the different environments. We will also characterize the SFR–mass relation, to see whether or not galaxies with different Hα properties and experiencing different physical processes are located in different regions of this plane. Finally, for spiral galaxies—for which disk galaxy sizes are meaningful—we will investigate if the Hα emission follows the extension of the disk, indicative of galaxies forming stars in the secondary component.

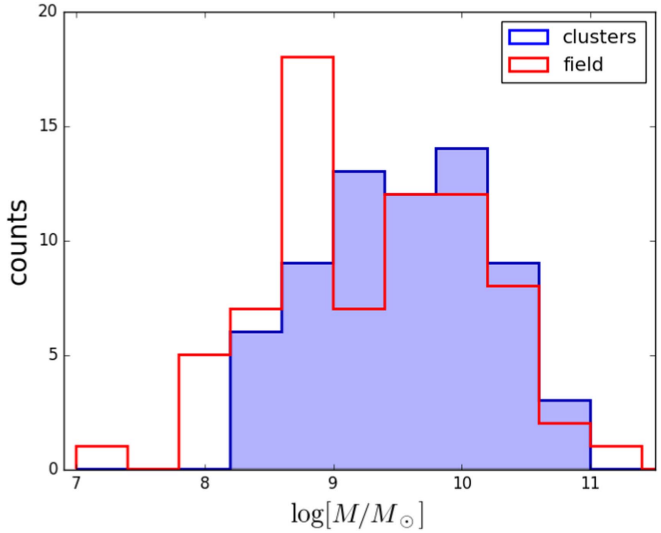

Figure 5. Stellar mass distribution for cluster (blue) and field (red) galaxies in our sample. Galaxies in the two environments are characterized by very similar mass distributions. Therefore, any differences in star formation properties between the two samples are not driven by differences in stellar mass.

Given the GLASS strategy (spectroscopic redshifts mainly for galaxies with emission lines) and the way our samples have been selected (visual selection), a statistical analysis on the incidence of Hα emitters in the different environments is not currently possible, and we therefore do not investigate the frequency of the Hα emitters with respect to the overall population in clusters and field.

4.1. The Peculiar Morphology of Hα Emitters

Figure 6 summarizes the morphological percentages for galaxies in clusters and in the field, for Hα emitter and non-Hα emitter galaxies. The two samples present morphological distributions that are all consistent within the 1σ errors: the Hα emitters are dominated by spiral galaxies, both in clusters ($41\% \pm 8\%$) and in the field ($51\% \pm 8\%$), followed by merging systems ($28\% \pm 8\%$ in clusters, $31\% \pm 7\%$ in the field). Ellipticals constitute $22\% \pm 7\%$ of the Hα emitter population in clusters, and $13\% \pm 6\%$ in the field. In both environments, S0s represent less than 7% of the entire population and they are slightly more numerous in clusters, in agreement with Dressler et al. (1997) and Postman et al. (2005). Irregulars represent just a few percent of the total population. We stress that among the Hα emitters, the fraction of both mergers and early-type (elliptical+S0) galaxies is remarkably high. Although this was somewhat expected for mergers, it is perhaps surprising for the early-type galaxies. Understanding the origin of star-forming ellipticals is beyond the scope of this work and will be revisited in future work.

In the control sample of non-Hα emitters, there is no predominance of a unique morphological class, with spirals constituting $28\% \pm 4\%$ of the total population in clusters and $31\% \pm 7\%$ in the field, ellipticals $38\% \pm 5\%$ in clusters, and $36\% \pm 7\%$ in the field. The incidence of merging systems is significantly less than among Hα emitters ($7\% \pm 3\%$ in clusters, $10\% \pm 3\%$ in the field), while irregulars are more

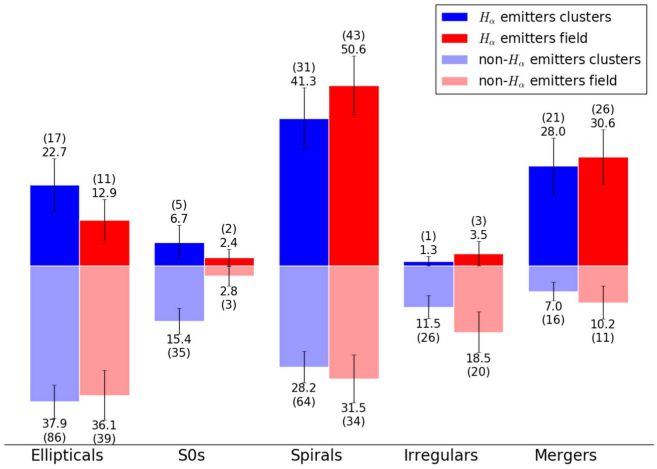

Figure 6. Morphological percentages of galaxies in clusters (blue) and in the field (red) for Hα emitters (darker colors, upper histograms) and non-Hα emitters (lighter colors, bottom histograms). Numbers represent percentages, error bars represent 1σ binomial errors (Gehrels 1986). Numbers in brackets give the number of objects in each class. Spiral galaxies dominate the population of Hα emitters, followed by merging systems. Interestingly, many Hα emitters have an early-type (S0+elliptical) morphology. In the control sample, there is no predominance of one morphological types, and the fraction of passive spirals is surprisingly high, compared to previous works (e.g., Poggianti et al. 2009).

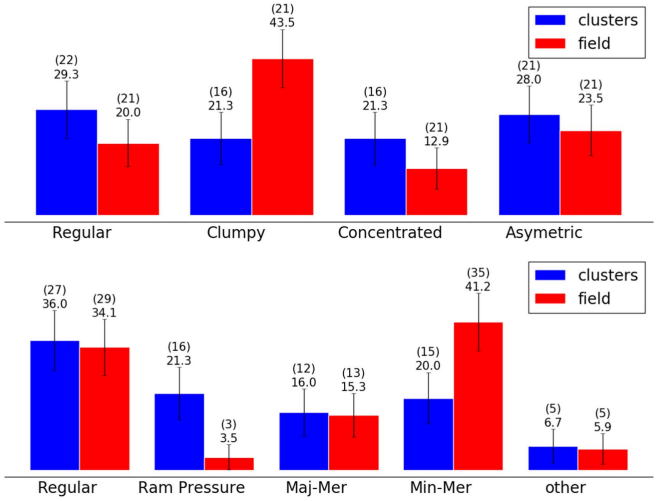

Figure 7. Hα morphology (upper panel) and proposed main process responsible for such morphology (bottom panel) percentages for Hα emitters in clusters (blue) and in the field (red). Numbers represent percentages, error bars represent 1σ binomial errors (Gehrels 1986). Numbers in brackets give the number of objects in each class. All morphologies and processes are well represented, consistent with a diversity of mechanisms being responsible for the morphology of Hα in these systems.

numerous (12% $\pm$ 3% in clusters, 19% $\pm$ 6% in the field). However, we caution the reader that in many cases it has been very difficult to distinguish between these two classes. It is very interesting to note the presence of such a high number of spiral and irregular galaxies that do not present Hα in emission above our Hα surface brightness detection limit of 5×10^{-2} $M_\odot$ yr^{-1} kpc^{-2}, indicating that, despite their morphology, these object are already passive, perhaps on their way to becoming lenticular galaxies (e.g., Ellis et al. 1997; Treu et al. 2003; Moran et al. 2005).

4.2. The Diversity of the Hα Morphologies

Having established that Hα emitters are a peculiar subsample of the entire galaxy population, we focus on the properties of these galaxies, and compare the broad band morphology to the morphology of the Hα line. We will pay particular attention to spiral galaxies, which represent the most common class of emitters, both in clusters and in the field.

Figure 7 presents the incidence of each Hα morphological class (upper panel) and process likely to be responsible for the observed Hα morphology (bottom panel), in both environments separately. We stress that that classification of the process label should be interpreted as qualitative and the adopted label is short-hand for what it is likely to be complex and not necessarily unique mechanisms.

We find that there is no dominant morphology for the Hα emission, and all the classes are almost uniformly populated. The only exception is the predominance of the clumpy Hα morphology in the field (44% $\pm$ 8%). Overall, this result is consistent with a diversity of factors affecting galaxy star-forming regions and therefore the Hα morphology. The other percentages agree within the errors, but in clusters there seems to be a larger number of galaxies with regular (30% $\pm$ 8% versus 20% $\pm$ 7% in the field), asymmetric (28% $\pm$ 8% versus 23% $\pm$ 7% in the field), and more concentrated (21% $\pm$ 7% versus 13% $\pm$ 6% in the field) Hα morphology.

Different physical processes might be acting on the different galaxies and the bottom panel of Figure 7 shows that in both environments star formation seems to proceed regularly and more or less undisturbed on $\sim$35% of the galaxies and none of the proposed process seems to be the responsible for the Hα morphology for $\sim$6% of the galaxies. The most common classification in clusters seems to be ram-pressure stripping, with 21% $\pm$ 7% of all galaxies falling in this category. In contrast, in the field, only 4% $\pm$ 3% of galaxies show signs of possible stripping. Major mergers seem to have a similar incidence in both environments (15% $\pm$ 7%), while minor mergers are by far more common in the field (41% $\pm$ 8%) than in clusters (20% $\pm$ 7%).

We note that fractions do not depend on stellar mass: the mass distributions of the different Hα morphological classes are very comparable, as are also those of galaxies classified as undergoing different physical processes.

It is interesting to note how the fraction of galaxies classified as minor mergers in the two environments is the same as the fraction of galaxies with a clumpy Hα morphology, suggesting a physical link between minor merging and Hα morphology. However, to understand the connection between process label and Hα appearance we must inspect the galaxy properties simultaneously, as done in Figures 8 and 9.

Figure 8 presents the incidence of galaxies of a given broad-band morphology and given Hα morphology, for the two environments separately. Numbers refer to the percentages with respect to the total population of Hα emitters in a given environment, and colors provide the information on the percentages of a given Hα morphology for each morphological class separately, e.g., the fraction of cluster galaxies with regular Hα morphology among elliptical galaxies. We warn the reader that when splitting the samples into many subgroups, uncertainties become important and prevent us from reaching solid conclusions.

Some trends emerge and there are interesting differences between the two environments. In clusters, elliptical galaxies

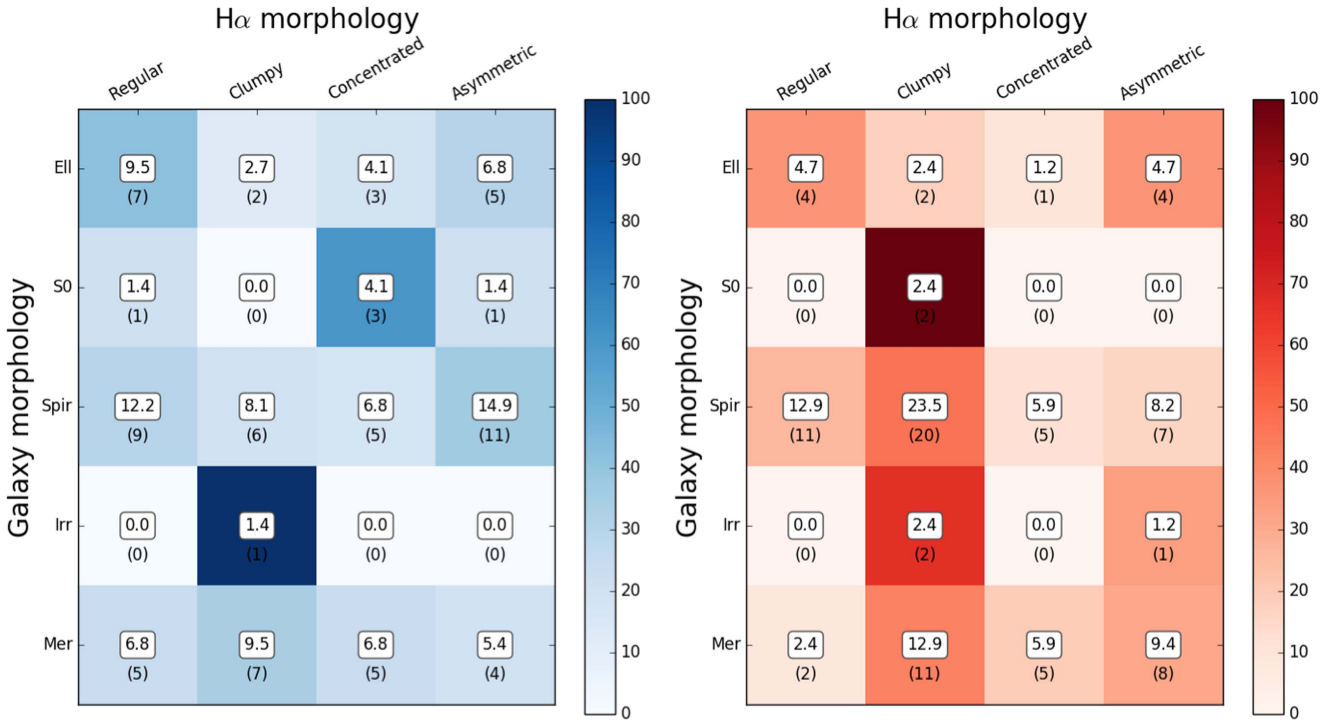

Figure 8. Percentages of galaxies of a given broad band morphology and Hα morphology in clusters (left panel) and in the field (right panel). The numbers shown represent the fraction of objects of a given Hα -galaxy morphology combination, i.e., the sum to 100. Numbers in brackets give the number of objects in each class. The color coding in the rows represents the percentages of a given Hα morphology for each morphological class separately. For instance, from the color bar, we see that ∼40% of spirals in the clusters have asymmetric Hα morphologies and that this combination makes up 14.7% of the full sample. The same class of objects make up 8.2% of the field galaxies, but only represent ∼10% of all spirals, as clumpy Hα dominates the spiral field sample.

most likely present a regular Hα morphology (9% ± 5% of all galaxies, ∼40% of elliptical galaxies), but in a few cases they present also the other Hα morphologies. In the field, ellipticals have the same chance of having a regular or asymmetric Hα morphology (5% ± 4% of the total, ∼40% of all ellipticals). Besides being a small fraction of the total sample, S0s in clusters most likely have concentrated Hα, while in the field they have a clumpy Hα distribution. Spiral galaxies have all kinds of Hα morphologies, but in clusters they have mostly asymmetric Hα (15% ± 6%), while in the field they have by far clumpy Hα (24% ± 7%). As expected, in both environments irregular galaxies do not have regular or concentrated Hα disk, but it is either clumpy or asymmetric. Finally, merging systems have all kinds of Hα morphologies, with a preference for clumpy morphology in the field (13% ± 6%), followed by the asymmetric one (9% ± 5%). It is interesting to note though that, especially in clusters merging systems can maintain a regular Hα morphology (∼30% of all mergers).

Similarly, Figure 9 presents the incidence of galaxies of a given Hα morphology classified as experiencing a given process, for the two environments separately. Again numbers refer to the percentages with respect to the total population of Hα emitters in a given environment, colors provide the information on the percentages of a given Hα morphology for each physical process separately; e.g., the fraction of galaxies with asymmetric Hα morphology among galaxies that are classified as likely experiencing ram-pressure stripping.

Overall, 25% ± 7% of galaxies in clusters present a regular Hα morphology and have regular star formation. This percentage is 18% ± 6% in the field. In both environments, a regular label is also associated with a concentrated Hα morphology, perhaps suggestive of a nuclear starburst without major outside disturbances, even though this case is not very common (∼6-8% of all galaxies, <30% of galaxies classified as regular). In clusters, the second most populated class is that of galaxies with asymmetric Hα classified as affected by ram-pressure stripping (18% ± 7% of the total population and >90% of galaxies likely experiencing this process). In a few cases ram pressure seems to produce a concentrated Hα morphology (3% ± 3%). In this case, we could be witnessing the final stage of a stripping event, when the galaxy is left with a truncated Hα disk. As expected, ram pressure is not very effective in the field (<4%). In clusters, major and minor mergers seem to produce all the different Hα morphologies, with a slight preference for the clumpy class. In contrast, in the field, 27% ± 7% of the total population have been classified as having clumpy Hα morphologies undergoing a minor merger and almost all minor mergers produce a clumpy Hα morphology (>90%). In the field, major mergers are less common events, and produce both clumpy (7% ± 4%) and asymmetric (6% ± 4%) Hα morphologies. Unidentified processes produce mainly clumpy Hα morphologies in clusters (4% ± 4%), and asymmetric Hα distribution in the field (5% ± 4%).

Unfortunately, due to a small number statistic, we cannot look for trends taking into account simultaneously all the three parameters (broad band morphology, Hα morphology, and process).

From the analysis above, based on our qualitative classification, it appears evident that our sample includes a large variety of objects with different properties and that different processes, representative of the different environments, can indeed produce similar features. Interestingly, in many cases the effect of the environment is hardly detectable, even with these sensitive tools

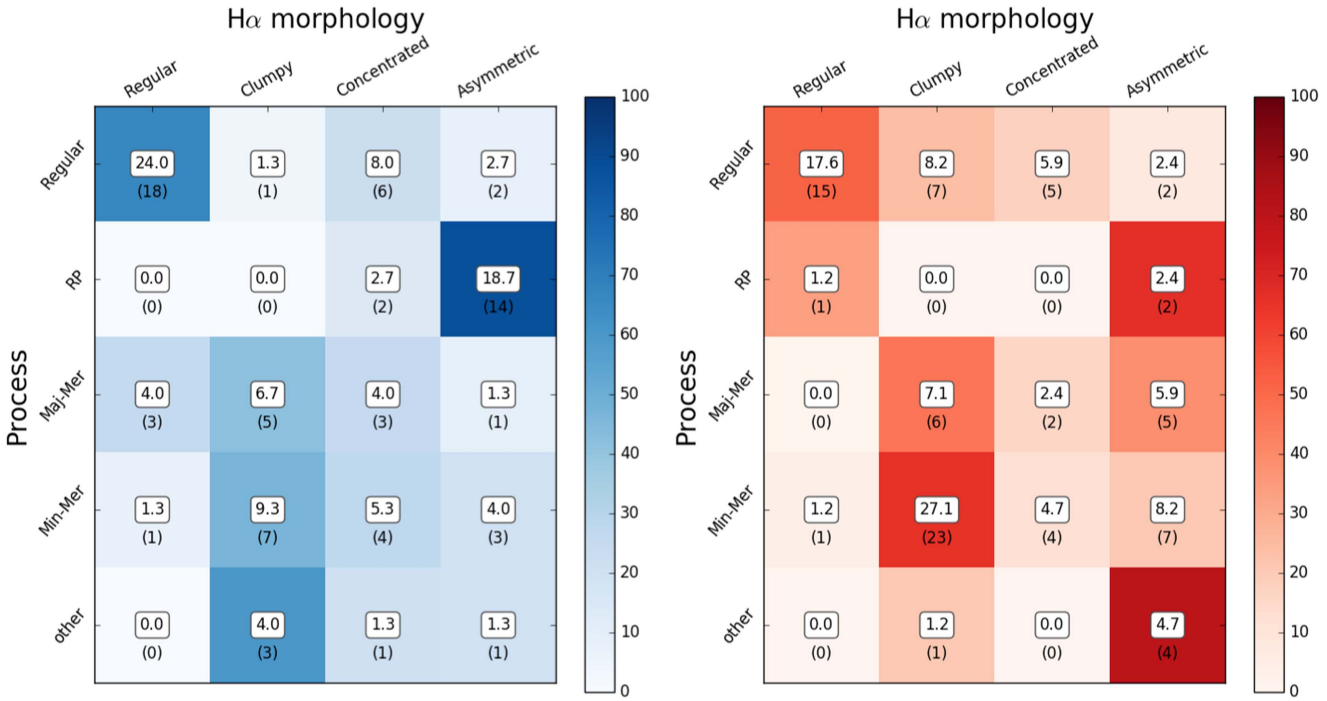

Figure 9. Similar to Figure 8, but comparing Hα morphology to the responsible processes. Again the left panel represents the cluster sample and the right panel shows the field sample.

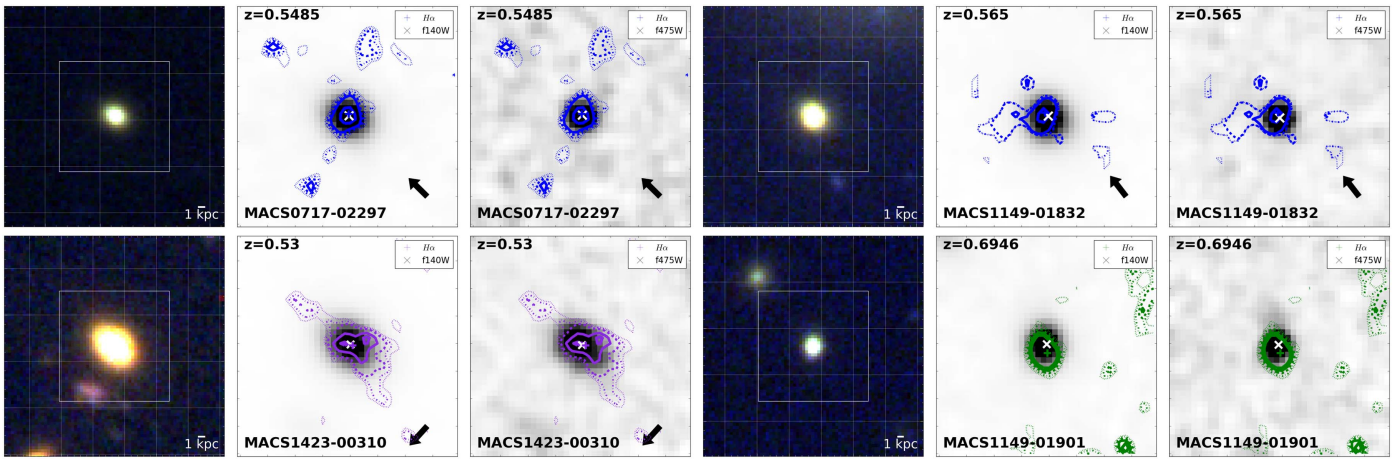

Figure 10. Example of galaxies with elliptical broad band morphology and detected Hα emission. For each galaxy, the left panel shows the color composite image of the galaxy based on the CLASH (Postman et al. 2012) or HFF (Lotz et al. 2016) *HST* data. The blue channel is composed by the F435W, F475W, F555W, F606W, and F625W filters, the green by the F775W, F814W, F850lp, F105W, and F110W filters, and the red by the F125W, F140W, and F160W filters. The central panel shows the Hα map superimposed on the image of the galaxy in the F140W filter and the right panel shows the Hα map superimposed on the image of the galaxy in the F475W filter. Contour levels represent the 35th, 50th, 65th, 80th, and 95th percentiles of the light distribution, respectively. Blue contours indicate that Hα maps are obtained from one spectrum, purple contours indicate that Hα maps are obtained from two orthogonal spectra, and green contours indicate that Hα maps are obtained by combining both the G102 and G141 grisms (only for $z > 0.67$). In the color composite image, the field of view is twice as big as the single-band images. A smoothing filter has been applied to the maps and an arbitrary stretch to the images for display purposes. For galaxies in clusters, arrows on the bottom right corner indicate the direction of the cluster center. The redshift of the galaxy is indicated on the top left corner.

and prior knowledge. This is consistent with the idea that environment-specific processes play a secondary role in galaxy evolution, at least for galaxies with $M_* > 10^8 M_\odot$. We now proceed by discussing in detail the most interesting classes.

4.3. Classes of Peculiar Objects

4.3.1. Elliptical Galaxies with Extended Hα in Emission

As mentioned above, 23(13)% of Hα emitters in clusters (field) present an elliptical morphology. This fraction is quite surprising since elliptical galaxies are generally thought to be quiescent (although blue cores have been seen in the past; Menanteau et al. 2005a, 2005b; Treu et al. 2005; Schawinski et al. 2009). Of these, in clusters ∼40% present a regular Hα morphology, ∼10% a clumpy Hα morphology, ∼20% a concentrated Hα morphology, and ∼30% an asymmetric morphology. The corresponding percentages for galaxies in the field are ∼35%, ∼20%, ∼10%, and ∼35%, respectively. Figure 10 shows some examples of these galaxies. For each object, a composite image of the galaxy based on the CLASH (Postman et al. 2012) or HFF (Lotz et al. 2016) *HST* images is shown, along with the Hα map superimposed on the image of

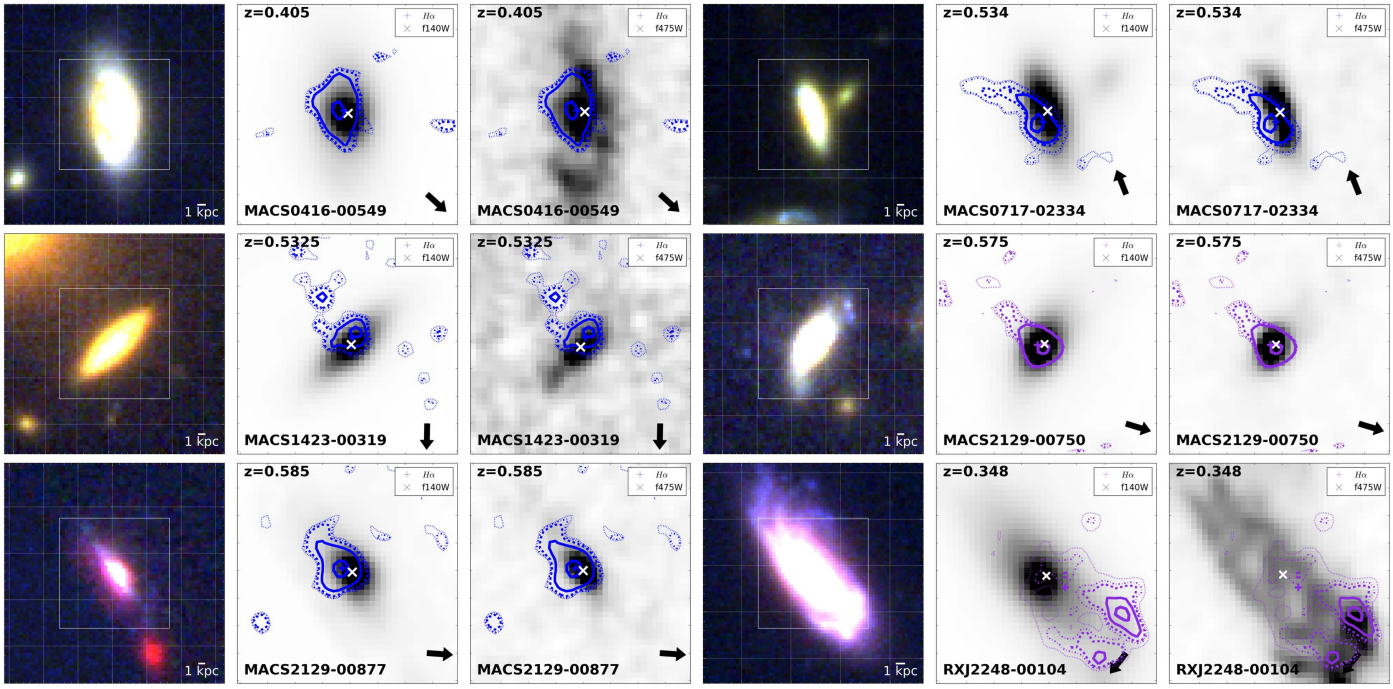

Figure 11. Example of galaxies with spiral morphology and asymmetric Hα mainly due to ram-pressure stripping. Panels, colors, lines, and labels are as in Figure 10.

the galaxy both in the F140W filter and in the F475W filter. As can be seen from the images, both the broad band morphology and the Hα emission are highly certain and therefore these are not spurious detections or misclassified objects. In clusters, four cases show clear signs of ram-pressure stripping (like MACS1149-01832, in the upper right panels of Figure 10), while there is only a tentative case of stripping in the field.

In both environments, these galaxies have a median SFR of $\sim 3 M_{\odot}$ yr^{-1}; field galaxies have a median mass of $\sim 10^{8.8} M_{\odot}$, and cluster galaxies of $\sim 10^{9.7} M_{\odot}$, and therefore they are not the most massive objects in our sample, but have a high SFR, suggesting they might actually be nuclear starbursts or AGNs. However, these galaxies do not all have concentrated Hα, indicating that even if present, the AGN cannot be entirely responsible for the detected Hα emission. In addition, the X-ray maps show that these elliptical galaxies are not strongly emitting in the X-ray, therefore the presence of strong AGNs is excluded.

The origin of these objects is unclear; they might be disk +bulge galaxies that have had their disk destroyed or removed by some process or very dusty objects. This class of objects will be revisited in a future work.

4.3.2. Spiral Galaxies with Asymmetric Hα Likely Due to Ram Pressure

Spiral galaxies are the most common class of Hα emitters, in both environments. In clusters, ∼35% of them show asymmetric Hα maps, corresponding to 15% of the total number of galaxies. In the field, 15% of all spirals show asymmetric Hα morphologies corresponding to 8% of all field Hα emitters. In clusters, in 65% of the cases the asymmetry has been classified as consistent with ram-pressure stripping; in the field this number is less than 30%. Figure 11 shows some examples. Most of them can be characterized as jellyfish galaxies, i.e., galaxies that exhibit tentacles of material that appear to be stripped from the galaxy, and whose morphology is suggestive of non-gravitational removal mechanisms, such as ram-pressure stripping (e.g., Ebeling et al. 2014; Fumagalli et al. 2014). Upon visual inspection, some of our galaxies really seem to be caught in the act of being stripped and are currently losing gas and material, producing a tail, which extends in the opposite direction of the cluster center. The bending of the Hα disk (e.g., for MACS0717-02334) might suggest that the galaxy is plunging into the ICM. We refer the reader to Paper VIII for a more detailed investigation of the relation between the Hα morphology and cluster properties. Interestingly, there are other galaxies (e.g., RXJ2248-00104) that seem to have already lost most of their Hα disk, which appears to be truncated. RXJ2248-00104 is a good example of multiple mechanisms as a merger, in addition to ram-pressure stripping, might be operating.

4.3.3. Spiral Galaxies with Clumpy Hα due to Mergers

In the field, almost 50% of spiral galaxies present a clumpy Hα morphology, while in clusters this fraction is less than 20%. In the field, in 80% of the cases this Hα morphology is attributed to the occurrence of minor mergers. Figure 12 shows some examples in the field. For almost all of these galaxies the F475W filter shows the presence of material infalling onto the main galaxies. This material is not detected in F140W, suggesting that, though luminous, it is not very massive. Therefore we classified it as minor mergers.

The median SFR of these galaxies is $\sim 3 M_{\odot}$ yr^{-1}, and the median mass is $10^{9.9} M_{\odot}$.

4.3.4. Galaxies with Concentrated Hα

The last class of objects that we single out for discussion is that made up of galaxies with very concentrated Hα. Galaxies of all morphologies enter this category, both in clusters and in

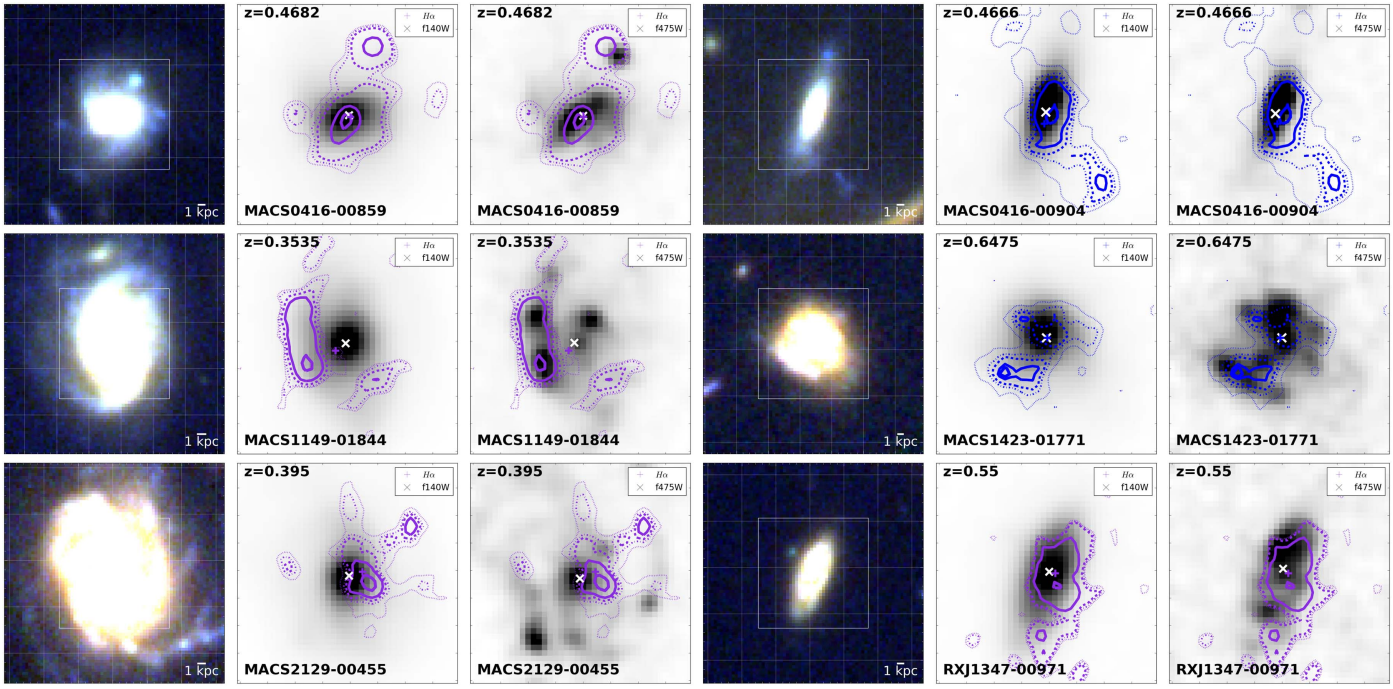

Figure 12. Example of galaxies with spiral morphology and clumpy Hα mainly due to minor mergers. Panels, colors, lines, and labels are as in Figure 10.

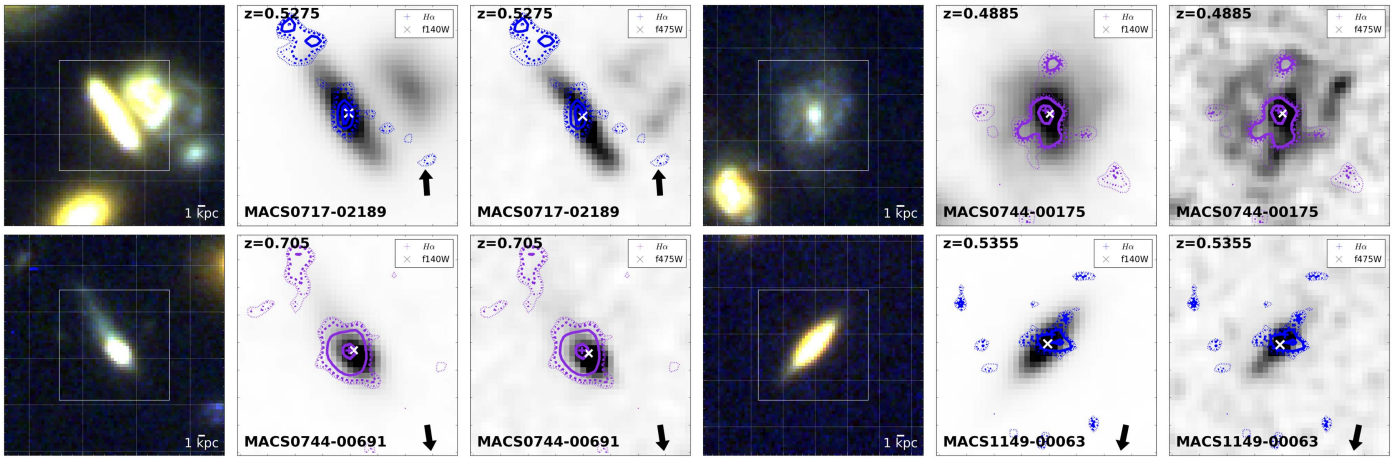

Figure 13. Example of galaxies with compact centrally located Hα . Panels, colors, lines, and labels are as in Figure 10.

the field, except that no S0s with concentrated Hα have been identified in the field. In clusters (field), regular diffuse star formation seems to be ongoing for 35% (45%) of the objects. The Hα disk seems fairly regular, though much smaller than the galaxy size, perhaps indicative of some other gentle process like strangulation, which is removing the most loosely bound gas. In the other cases, both minor and major mergers seem to induce a concentrated Hα morphology. Figure 13 shows some examples. It appears evident that some emission is more clumpy, and some very asymmetric.

4.4. Offsets between Hα and the Galaxy in the Continuum

In the analysis above, when comparing the Hα emission to the image of the galaxies in the continuum, we have neglected an important aspect: in many cases there seems to be an offset between the peak of the Hα emission and the peak in the continuum.

Comparing the position of the peak of the Hα emission to that of the continuum, as traced by the F475W,[14] we found that in both environments, for most of the galaxies the displacement is smaller than 1.5 kpc (plot not shown). The average offset is ∼0.5 kpc (typically 0.″05). We note that this offset is larger than any potential uncertainty in the astrometry for the different bands, which is of the order of a fraction of a pixel. For reference at the redshifts consider here, 1 pixel corresponds roughly to 0.2–0.3 kpc. The existence of the offset suggests that in most galaxies the bulk of the star formation is not uniformly diffused. Past and current star formation is not co-located, as for example assumed by Nelson et al. (2012, 2013, 2015).

These results confirm our previous findings, based only on two clusters (Vulcani et al. 2015).

Figure 14 gives the mean values of the distance between the peak of the Hα emission and the continuum (F475W filter), for

[14] For A2744 the F435W is used instead.

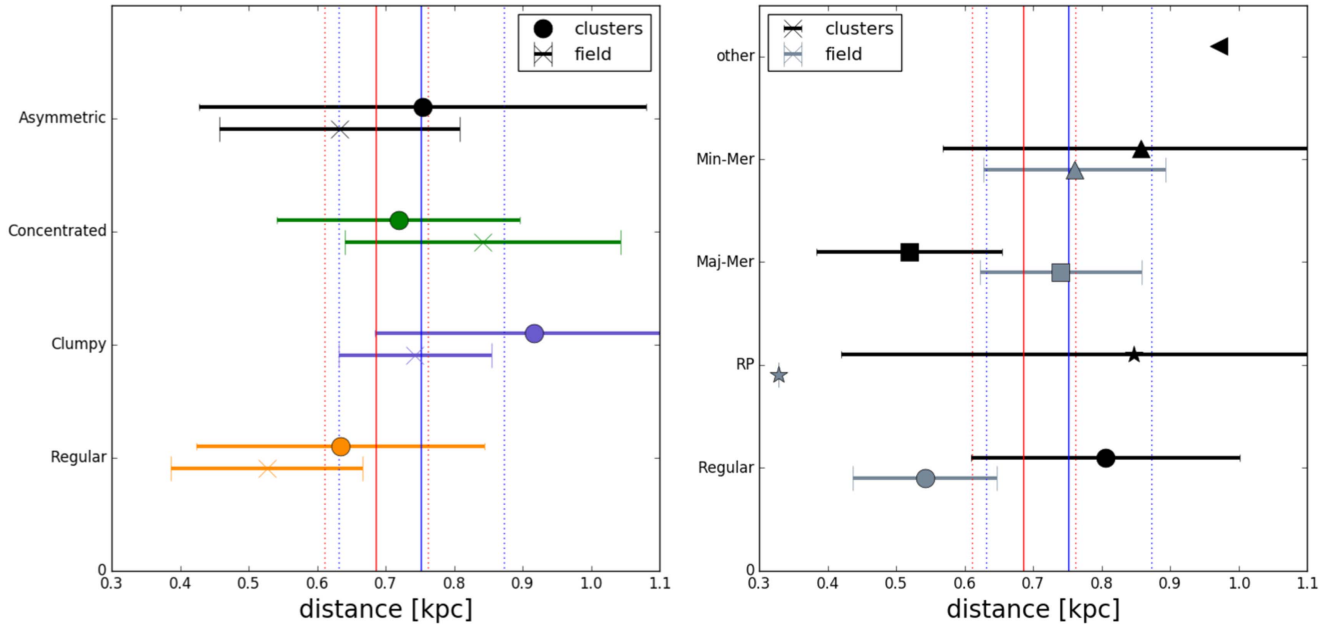

Figure 14. Mean values along with errors of the distance between the peak of the Hα emission and the continuum (F475W filter), for galaxies with both PAs. Left panel: galaxies in the field and clusters with different Hα morphologies, as indicated in the label. Right panel: galaxies in the field and clusters experiencing different processes, as indicated in the label. Vertical solid and dotted lines represent the means with errors for the total populations (blue lines for clusters, red lines for the field).

galaxies showing different Hα morphologies (left) and possibly feeling different physical processes (right). Only galaxies with both PAs are considered. Similar results are obtained for the two offsets separately. Values are in agreement within uncertainties, but there are hints that, e.g., galaxies with regular Hα morphologies have smaller offset than galaxies with a clumpy morphology (especially in clusters). In clusters, galaxies undergoing ram-pressure events tend to have larger offset, as do merging galaxies. Comparing the two environments, no robust systematic differences are detected.

4.5. Star Formation Rates

We can relate the results obtained so far to the position of the galaxies on the SFR–mass plane, to investigate whether we can establish a link between the specific SFR (or the SFMS) and environmental processes. Figure 15 shows our cluster and field galaxies, overplotted with the AEGIS Noeske et al. (2007) field galaxies and the EDisCS Vulcani et al. (2010) cluster galaxies, both at $z \sim 0.5$.

The GLASS samples span a wide redshift range ($0.3 < z < 0.7$), therefore the spread is expectedly due to the evolution of the SFR–M_* relation with z, but our sample is too small to investigate evolutionary trends.

The Noeske et al. (2007) sample is complete down to $\sim M^* > 10^{9.7}$ and logSFR > 0, while the Vulcani et al. (2010) sample is complete down to $\sim M^* > 10^{10.6}$ and similar SFRs. Therefore, the overlap between the GLASS and literature samples is limited. The GLASS galaxies tend to lay on the SFR–mass relation of blue galaxies with emission lines or detected in the infrared (see Noeske et al. 2007; Vulcani et al. 2010, for details on their sample selection), tracing the upper envelope. To some extent, this was expected given that our sample has been assembled by selecting visually detected Hα emitters, and thus preferentially rapidly star-forming galaxies.

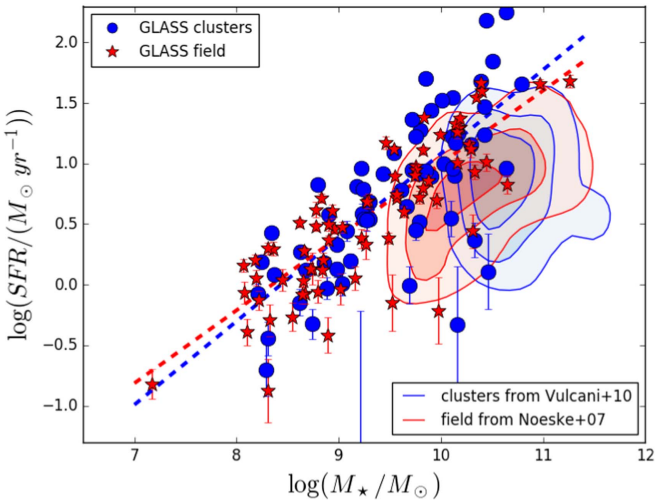

Figure 15. GLASS SFR–mass relation overplotted to the field relation (from Noeske et al. 2007) and the cluster relation at similar redshift (from Vulcani et al. 2010), both at similar redshift. Blue filled circles and dashed blue line: GLASS cluster galaxies and fit; red filled stars and dashed red line: GLASS field galaxies and fit. The typical error on stellar masses is 0.2 dex and not shown for clarity. Blue contours: EDisCS clusters; red contours: AEGIS field. For EDisCS and AEGIS, only blue emission line galaxies and galaxies detected at 24 μm above the mass and SFR completeness limits have been considered (refer to Noeske et al. 2007; Vulcani et al. 2010, for details on the sample selection).

Furthermore, it is important to note that the comparison with the literature is not straightforward. Noeske et al. (2007) and Vulcani et al. (2010) used long-slit spectroscopy and their SFR estimates are underestimated for extended galaxies, while GLASS, making use of slitless grism spectroscopy, gives a more reliable estimate for extended objects.

Our results show that at $0.3 < z < 0.7$ the vast majority of cluster galaxies can be as star forming as field galaxies of similar mass. In the literature, e.g., Patel et al. (2009), Vulcani

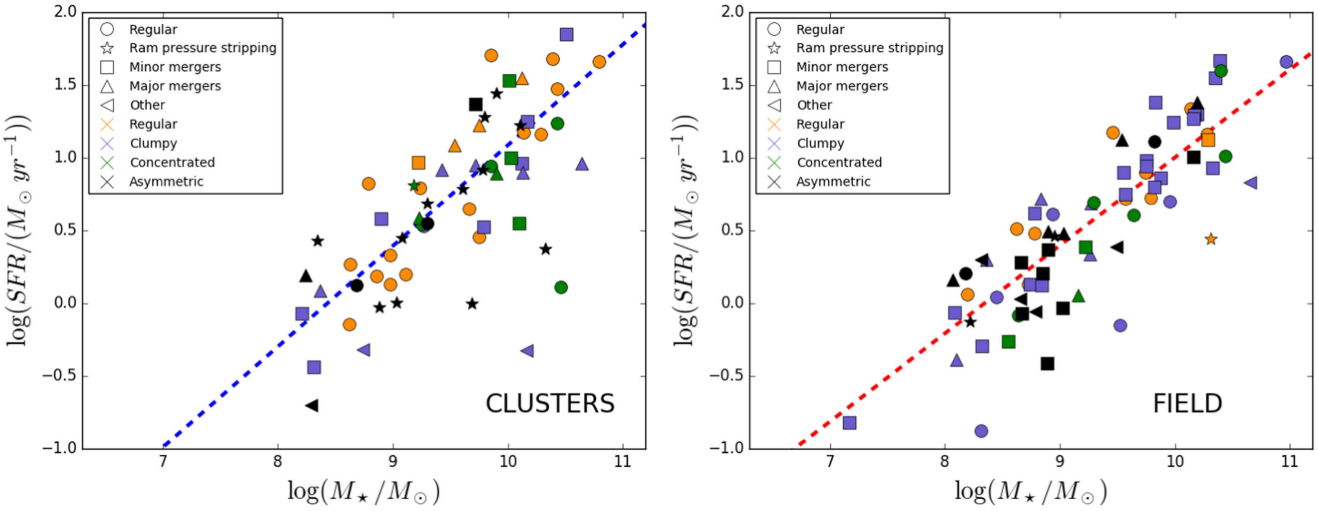

Figure 16. SFR–mass relation for galaxies of different Hα morphology and subject to different physical processes in clusters (left) and in the field (right). For the sake of clarity, error bars are not shown. The different symbols and colors are summarized in the label. Dashed lines represent the best-fit relation for clusters (blue, left) and field (red, right). No clear trend between Hα morphology and SFR: galaxies with comparable values of SFR can have very different Hα morphologies.

et al. (2010), Koyama et al. (2013), and Paccagnella et al. (2016), have detected both at these redshift and at $z \sim 0$ the existence of a population of galaxies with a reduced SFR at fixed stellar mass, which is absent in the field. These galaxies are most likely in transition from being star forming to being passive. Probably due to our limited number statistic, we are not able to firmly single out this population, even though few galaxies in our clusters indeed show a reduced SFR given their mass.

In order to investigate the connection between process and star formation, we then investigate whether or not galaxies with different Hα morphologies classified as experiencing different processes populate specific regions of the SFR–mass plane.

From broad band morphology (plot not shown), we find that the different classes are almost normally distributed around the fit, with elliptical galaxies presenting a large dispersion. Cluster galaxies in the low SFR tail are spirals, while two of them are ellipticals.

Figure 16 presents the SFR–mass relation for galaxies of different Hα morphology subject to different physical processes in the two environments separately We note that there is no clear trend between Hα morphology and SFR: galaxies with comparable values of SFR can have very different Hα morphologies. Nonetheless, some tentative trends emerge.

Interestingly, cluster galaxies classified as undergoing ram-pressure stripping (stars) seem to be located both above and below the SFR–mass relation, showing how star formation is either enhanced in these systems (in agreement with Poggianti et al. 2016), or suppressed, when we are witnessing a late stage of the phenomenon. As already mentioned, most of these galaxies show an asymmetric Hα morphology and some of them look like jellyfish galaxies.

Major mergers (triangles) seem to induce an enhancement of the star formation, in clusters and also in the field. Overall, cluster galaxies in the tail of low SFR have Hα concentrated and are produced by unidentified ("other") processes. In clusters, galaxies with Hα concentrated (green symbols) are found only for $M_* > 10^9 M_*$. Galaxies showing a regular Hα morphology (circles) and experiencing regular processes (orange symbols) tend to be located above the best fit of SFR–mass relation.

Even though we have used arguably one of the most sensitive diagnostic tools for trying to interpret the SFR–mass relation, we could not find any clear trend within the SFR–mass plane. It is possible that any trends within the plane are obfuscated by uncertainties in our classification scheme or perhaps our sample is not large enough. However, if the effects on environmental processes on these integrated measures had been dramatic we should have been able to see them. The lack of clear trends is thus consistent with the idea that environmental process play a secondary role in establishing the SFR for a galaxy of a given mass.

Nelson et al. (2015) have also related the spatial extent of the Hα distribution and stellar mass, by stacking Hα images to reach deep surface brightness limits ($\sim 10^{-18}$ erg s^{-1} cm^{-2} arcsec^{-2}) for field galaxies at $z \sim 1$. They mapped the Hα distribution as a function of SFR(IR+UV) and found that above the main sequence Hα is enhanced at all radii; below the main sequence Hα is depressed at all radii. This suggests that at all masses the physical processes driving the enhancement or suppression of star formation act throughout the disks of galaxies. For $10^{10.5} < M_*/M_\odot < 10^{11}$, above the main sequence, they found that Hα is particularly enhanced in the center, indicating that gas is being funneled to the central regions of these galaxies to build bulges and/or supermassive black holes. Below the main sequence, the star-forming disks are more compact.

In contrast, Willett et al. (2015) have analyzed the local SFMS of disk galaxies and found that it is remarkably robust to the details of the spatial distribution of star formation within galaxies. They classified galaxies in a wide range of morphological sub-types, i.e., number or pitch angle of spiral arms, presence of a large-scale bar; but did not detect any statistically significant difference in the relative position of these sub-types across the SFMS. They concluded that system that regulates star formation in galaxies is thus either not affected by the details of the spatial distribution of star formation, or its regulatory effect is so strong that it wipes out any such effect in a short time.

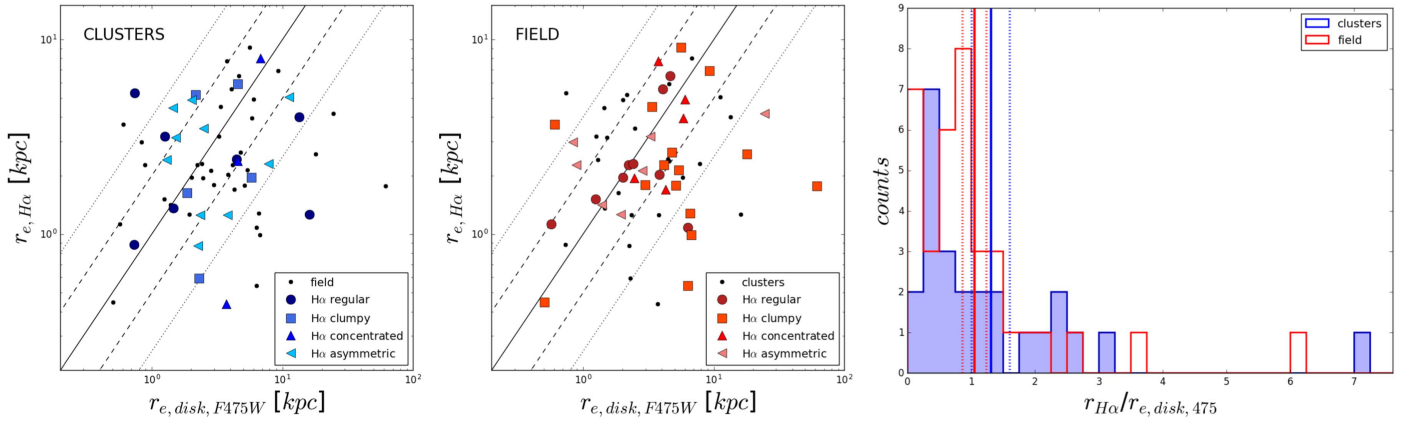

Figure 17. Size comparisons for spiral galaxies in our sample, for which the assumption of the existence of the disk holds. Left panel: Hα size vs. F475W size for cluster galaxies. Galaxies with different Hα morphologies are highlighted, as indicated in the label. Lines show the 4:1, 2:1, 1:1, 1:2, and 1:4. Small black dots are field galaxies, for comparison. Central panel: Hα size vs. F475W size for field galaxies. Galaxies with different Hα morphologies are highlighted, as indicated in the label. Lines show the 4:1, 2:1, 1:1, 1:2, and 1:4. Small black dots are cluster galaxies, for comparison. Right panel: distribution of the ratios of Hα size to the F475W size, for galaxies in clusters (blue, filled histogram) and in the field (red, empty histogram). Mean values along with 1σ errors are also indicated. The mean ratio between Hα size and size in the continuum (F475W) is close to 1, in both environments, indicating that Hα traces the disk and suggesting that indeed star formation is mainly taking place in this component. Galaxies with different Hα morphology are not strongly clustered in the size–size plane, even though concentrated objects tend to have smaller Hα size, in both environments. In clusters, a population of galaxies with Hα much larger than the size in the continuum tends to appear, maybe an indication that these galaxies are currently ram-pressure stripped.

4.6. Comparison between Sizes in Different Bands for Spiral Galaxies

As discussed in Section 3.5, we have measured sizes for all the galaxies, assuming a double profile fit for the galaxies in the continuum, and a single profile fit with $n = 1$ for Hα maps. The former assumption is valid for galaxies with a regular morphology, such as ellipticals (which are supposed to have a negligible second component), S0s, and spirals. The latter assumption is valid under the hypothesis that the Hα is distributed across a disk. As we have seen so far, these assumptions are valid only for a fraction of galaxies in our sample, while the rest show non-canonical morphologies and host very irregular Hα distributions.

In what follows, we will consider only spiral galaxies and investigate whether in these objects Hα actually follows the disk, indication that star formation is taking place in this component, or whether the two portions of the galaxies are uncorrelated. To do so, we compare the size of Hα to the size of the disk of the galaxy, measured both from the F475W filter and the F140W filter. These two filters capture the light of two different stellar populations: the former is more sensitive to the younger population (SFR in the last million years), while the latter is more sensitive to the older stellar component.

The left and central panels in Figure 17 compare the size of the Hα disk to the size of the galaxy disk at F475W for cluster and field galaxies separately. Galaxies with different Hα morphology are also highlighted. The right panel shows the distribution of the ratio of sizes at the different wavelengths.

Cluster and field galaxies occupy slightly different regions of the plane: field galaxies seem to have systematically smaller Hα sizes compared to the continuum sizes, while in clusters there are outliers with Hα size much larger than the continuum size. These cluster galaxies might be likely experiencing ram-pressure stripping, which is puffing up the Hα disk (in agreement with our results presented in Vulcani et al. 2015).

Mean values peak around one, indicating that Hα is approximately on the same scale of the disk, indicating that most of the star formation indeed is occurring in the disk as assumed.

Interestingly, the Hα size is not strongly correlated to the Hα morphology: while some systematic differences are detected (e.g., if Hα is concentrated the Hα size is smaller) these are all within the observed scatter.

Using the F140W filter instead of F475W, no strong differences are detected (plots not shown), except that sizes in the continuum are systematically smaller, as expected given that we are looking at an older stellar population and the known color gradients in galaxies. Finally, for spiral galaxies, we can investigate how the SFR correlates with the size of the disk and its mass, to investigate whether or not the Hα disk and the galaxy disk coincide.

The correlation between SFR and size (left panel of Figure 18) is not very tight, in either environment. Overplotted are also lines of constant star formation density $\Sigma_{\rm SFR}$. Our galaxies do not lie on any of these tracks, spanning a range of almost two orders of magnitude in star formation density. We interpret this as the result of a diversity of modes of star formation, from different levels of star formation in disk with different supplies of cold, to perhaps nuclear starbursts or star formation associated with interactions and accretion.

Using the information on the B/T ratio, we can estimate the mass of the disk in galaxies ($M_{\rm disk} = (1 - B/T) \times M_*$). Especially for field galaxies, this relation is much tighter than the canonical SFR–mass relation for the same galaxies (plot not shown), suggesting that indeed the bulk of the star formation is occurring in disks.

Abramson et al. (2014) found that by normalizing galaxies by the stellar mass of the disk alone, the slope of the SFMS is consistent with only a linear trend (removing any dependence on mass). Although this correction to the disk stellar mass homogenizes the SFMS for disks with a range of B/T, the intrinsic dispersion (σSFR) of the sequence must be a result of contributions by bars, disk dynamics, halo heating, AGN activity, environment, and/or gas accretion history, among other factors (Dutton et al. 2010). While the overall bulge strength does affect the position of a galaxy on the SFMS (Martig et al. 2009; Cheung et al. 2012; Fang et al. 2013; Kaviraj 2014; Lang et al. 2014; Omand et al. 2014), the

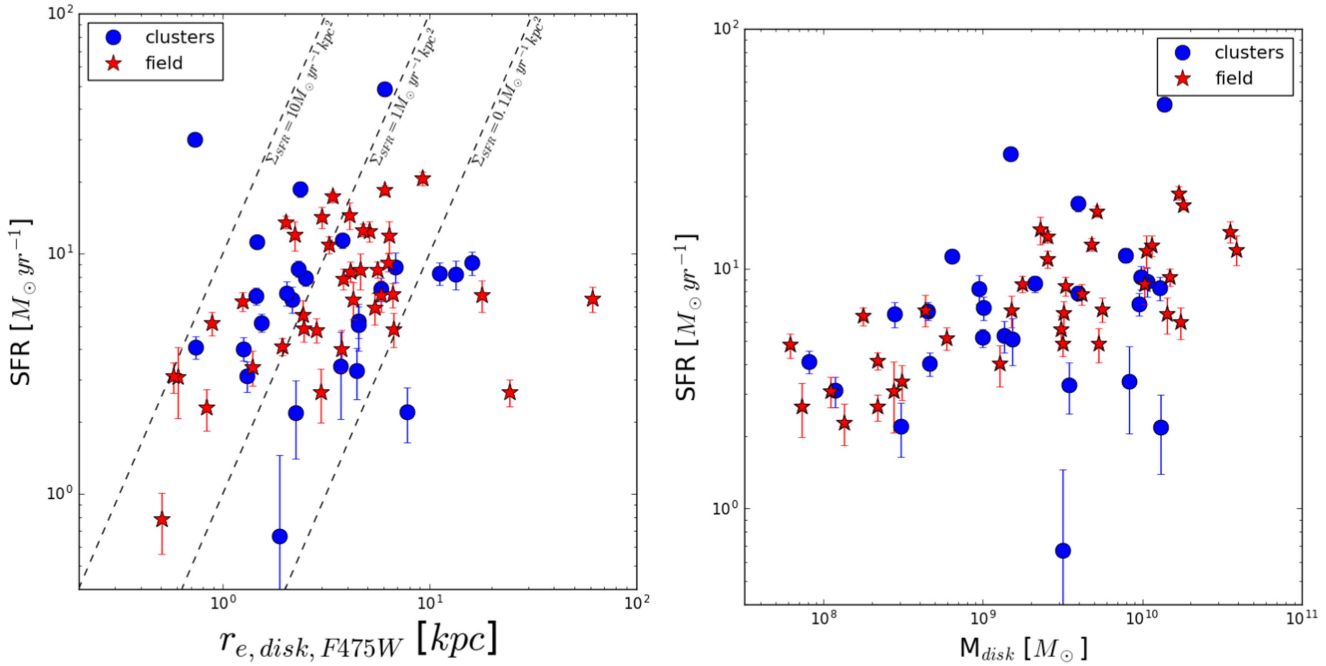

Figure 18. Left: SFR-size disk relation for spiral galaxies in clusters (blue circles) and in the field (red stars). Dashed lines indicate the loci of constant SFR density. Right: SFR–mass disk relation for spiral galaxies in clusters (blue circles) and in the field (red stars).

structure of the disk itself does not (Willett et al. 2015). These findings are consistent with recent models in which details of the feedback, which also relate strongly to the galaxy properties, have little effect on the SFMS (Hopkins et al. 2014). Alternatively, this also agrees with models in which the SFMS is the result of stochastic processes, rather than deterministic physics related to galaxy evolution (Kelson 2014).

5. DISCUSSION AND CONCLUSIONS

Building on our pilot study presented in Vulcani et al. (2015), we have continued our exploration of the spatial distribution of star formation in galaxies at $0.3 < z < 0.7$, as traced by the Hα emission in the field of view of the 10 GLASS clusters, detailing and strengthening our previous results. We have produced Hα maps, taking advantage of the WFC3 G102 and WFC3-G141 data at two orthogonal PAs. We visually selected galaxies with Hα in emission and, based on their redshift, assigned their membership to the cluster. We used galaxies in the foreground and background of the clusters to compile a field sample at similar redshift. The cluster and field samples are well matched in stellar mass and have very similar data quality, ensuring that any differences in the populations are not driven by the stellar mass of the galaxies or instrumental selection effects.

We have visually classified both field and cluster galaxies, paying particular attention to their broad band morphology, the Hα morphology. We have introduced a new scheme to visually categorize galaxies according to the main process that are affecting the mode of star formation. Our is clearly a qualitative and approximate classification scheme, considering that multiple processes might be simultaneously at work, but we believe there is merit in categorizing in a self-consistent manner the diversity of morphological features across environments. More quantitative tests on the ability of detecting ram-pressure stripping effect are currently underway (Paper VIII).

We have correlated these quantities to the extent of the Hα emission and its position within the galaxy, in order to present a complete characterization of the Hα emitters in different environments.

The main results of this analysis can be summarized as follows.

1. Comparing the morphological distribution of Hα emitters to that of a reference sample matched in mass and environment, we found systematic differences: among the Hα emitters, 40% of galaxies in clusters and 50% of galaxies in the field present a spiral morphology. In both environments, the second most common morphological class is that of mergers, followed by ellipticals and S0s. In contrast, in the control sample, there is no dominant morphological type, with ellipticals and spirals the most represented ones.
2. Hα emitters can assume a variety of Hα morphologies consistent with a diversity of physical processes. Nonetheless, some patterns have been found. In the field Hα emitters most likely present a clumpy Hα morphology consistent with minor mergers or accretion (27% of the galaxies), or a regular morphology where current star formation appears to be co-located with past star formation (18%). Perhaps surprisingly, regular galaxies not affected by any strong process are the most common class in clusters (25%), followed by asymmetric galaxies where clear signs of ram-pressure stripping have been detected (18%). The most common process label in clusters is ram pressure, while in the field it is mergers, mostly minor.
3. Comparing the position of the peak of the Hα emission to that of the continuum, as traced by the F475W filter, we found that in both environments, for most of the galaxies the displacement is smaller than 1.5 kpc and the average offset is $\sim$0.5 kpc. The existence of the offset suggests that current star formation is not generally co-located with recent star formation, perhaps as the result of

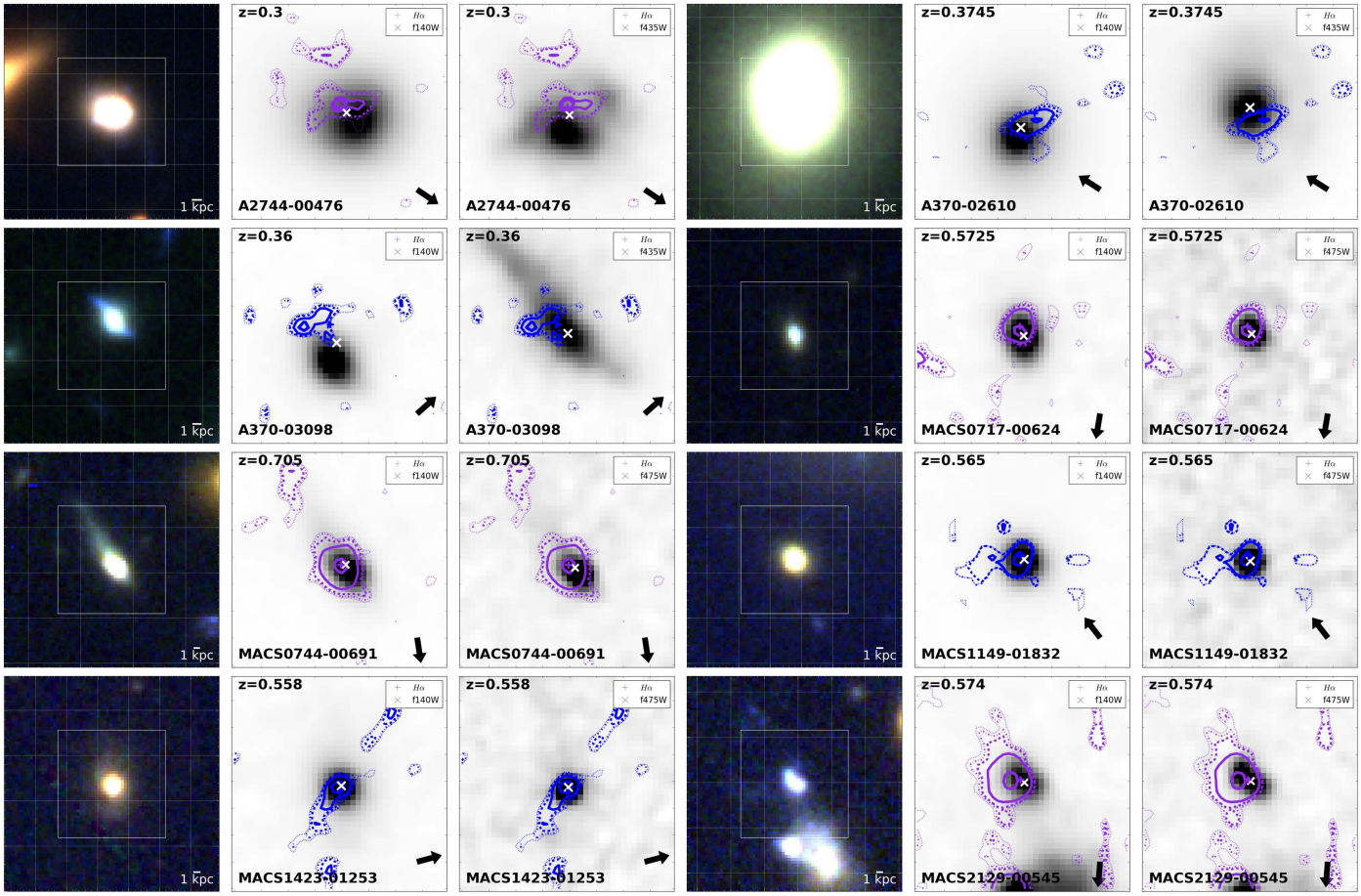

Figure 19. Cluster galaxies labeled as ram-pressure stripping candidates according to our classification scheme (Section 3.6). For each galaxy, the left panel shows the color composite image of the galaxy based on the CLASH (Postman et al. 2012) or HFF (Lotz et al. 2016) *HST* data. The blue channel is composed by the F435W, F475W, F555W, F606W, and F625W filters, the green by the F775W, F814W, F850lp, F105W, and F110W filters, and the red by the F125W, F140W, and F160W filters. The central panel shows the Hα map superimposed on the image of the galaxy in the F140W filter and the right panel shows the Hα map superimposed on the image of the galaxy in the F475W filter. Contour levels represent the 35th, 50th, 65th, 80th, and 95th percentiles of the light distribution, respectively. Blue contours indicate that Hα maps are obtained from one spectrum, purple contours indicate that Hα maps are obtained from two orthogonal spectra, and green contours indicate that Hα maps are obtained combining both the G102 and G141 grisms (only for $z > 0.67$). In the color composite image, the field of view is twice as big as the single-band images. A smoothing filter has been applied to the maps and an arbitrary stretch to the images for display purposes. Arrows on the bottom right corner indicate the direction of the cluster center. The redshift of the galaxy is indicated on the top left corner.

accretion of satellites or gas, or non-gravitational interactions such as ram-pressure stripping affecting the spatial distribution of the cold gas.

4. Overall, cluster and field galaxies share a similar SFR–mass relation. Galaxies with different Hα morphologies produced by different processes may populate different regions of the SFR–mass plane, but due to our low number statistics we cannot draw firm conclusions. Galaxies likely experiencing a ram-pressure event are located either above the main sequence (SFR enhanced, maybe suggestive of ongoing stripping) or below (SFR suppressed, maybe suggestive of past stripping). Galaxies undergoing a major merger event tend to have SFR enhanced, both in clusters and in the field. In clusters, the tail at low SFR level is populated by clumpy or concentrated Hα morphologies, due to some unidentified process.
5. For spiral galaxies, we compared the size of the current star formation (traced by Hα) and the recent star formation (as traced by the disk in filter F475W). In general Hα traces the disk, with the mean size ratio being close to unity, in both environments. Galaxies with different Hα morphology are not strongly clustered in the Hα size–$r_{\rm e,disk}$ size plane, even though concentrated objects tend to have smaller Hα size, in both environments. In clusters, a population of galaxies with Hα much larger than the size in the continuum tend to appear, consistent with their gas being currently being stripped or disturbed by environmental processes.

The emerging picture is that Hα emitters are a very heterogeneous population, characterized by a range of morphologies, sizes, and SFRs, in agreement with previous studies conducted from the ground (e.g., Yang et al. 2008; Gonçalves et al. 2010; Swinbank et al. 2012; Sobral et al. 2013; Wisnioski et al. 2015; Stott et al. 2016) and from space (Nelson et al. 2012, 2013, 2015). Therefore, a simple explanation cannot describe our observations. Even though we identified some small systematic differences between galaxies in the field and in clusters, both populations present very mixed morphologies and experience a variety of processes.

Non-gravitational interactions such as ram-pressure stripping seem to play an important role in clusters while it is much less effective in the field. This is in agreement with previous studies that showed how this phenomenon is expected to be important at

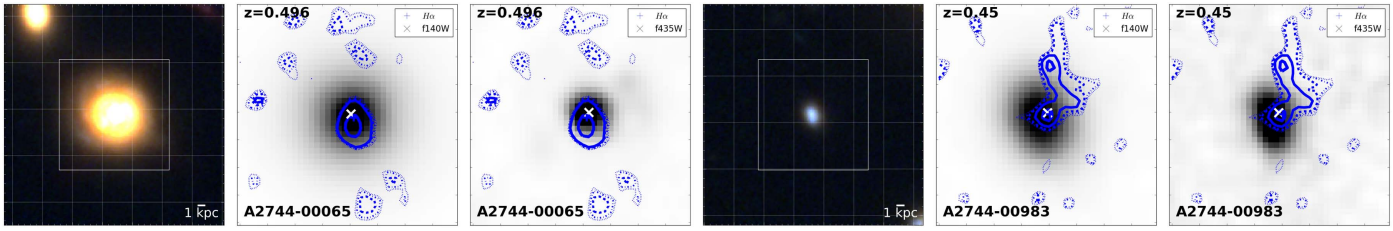

Figure 20. Field galaxies labeled as ram-pressure stripping candidates according to our classification scheme (Section 3.6). For each galaxy, the left panel shows the color composite image of the galaxy based on the CLASH (Postman et al. 2012) or HFF (Lotz et al. 2016) *HST* data. The blue channel is composed by the F435W, F475W, F555W, F606W, and F625W filters, the green by the F775W, F814W, F850lp, F105W, and F110W filters, and the red by the F125W, F140W, and F160W filters. The central panel shows the Hα map superimposed on the image of the galaxy in the F140W filter and the right panel shows the Hα map superimposed on the image of the galaxy in the F475W filter. Contour levels represent the 35th, 50th, 65th, 80th, and 95th percentiles of the light distribution, respectively. Blue contours indicate that Hα maps are obtained from one spectrum, purple contours indicate that Hα maps are obtained from two orthogonal spectra, and green contours indicate that Hα maps are obtained combining both the G102 and G141 grisms (only for $z > 0.67$). In the color composite image, the field of view is twice as big as the single-band images. A smoothing filter has been applied to the maps and an arbitrary stretch to the images for display purposes. The redshift of the galaxy is indicated on the top left corner.

the center of massive clusters because of the large relative velocities and higher densities of the ICM (Gunn & Gott 1972; Quilis et al. 2001; Font et al. 2008; Bekki 2009). Brüggen & De Lucia (2008) showed that virtually all cluster galaxies suffered weaker episodes of ram pressure, suggesting that indeed this physical process might play a significant role in shaping the observed properties of the cluster galaxy population. They also found that ram pressure fluctuates strongly such that episodes of strong ram pressure are followed by two episodes of weaker ram pressure, possibly allowing the gas reservoir to be replenished and intermittent episodes of star formation to occur. In agreement with this, in our sample we detected a broad range of ram-pressure strengths affecting the GLASS galaxies. We also detected stripping in galaxies of different broad band morphology, consistent with the idea that gas stripping does not directly and instantaneously affect galaxy morphology.

We found that galaxy mergers and more generally major galaxy–galaxy interactions are frequently detected in field Hα emitters, and less in massive clusters, where the large velocity dispersions impede encounters (e.g., Mihos & Hernquist 1996). As expected, we found that mergers trigger star formation. Interestingly, Sobral et al. (2011) found instead that the increase in mergers within Hα emitters is progressive from field into groups and into clusters. Their analysis revealed that non-merger-driven star formation is strongly suppressed in both rich groups/cluster environments and for high stellar masses, implying that once potential mergers are neglected, stellar mass and environment both play separate and important roles.

Broadly speaking, we conclude that the effects of cluster-specific mechanisms on galaxy evolution are detectable in our unprecedented data. However, they are both subtle and complex. They are subtle in the sense that no dramatic trend is found between the morphology of the current star formation and the environment or other properties of the galaxy. Every trend that we have found is weak and there are always exceptions. This is consistent with previous work based on spatially unresolved data that has concluded that the differences are small, once one controls for stellar mass and other parameters directly related to the time of initial collapse of the halo in which the galaxy is found (Morishita et al. 2016). They are complex in the sense that the richness of morphologies and sizes and relationships between current, recent, and past star formation cannot be easily reduced to a small number of clear-cut categories. This complexity limits the extent to which data of this quality can be interpreted in the absence of full-blown quantitative calculations of these effects. The dynamical range, resolution, and physical complexities that need to be rendered in order to carry out a detailed comparison between theory and data are stupendous. However, given recent progress in hydrodynamical numerical simulations (e.g., Illustris, Vogelsberger et al. 2014) it seems that detailed comparisons between the kind of data derived here and simulated maps would be an interesting exercise and might provide a way forward.

Another important issue that we have not addressed in this paper is how the properties of galaxies depend on the detailed properties of their host clusters. As discussed by Treu et al. (2015), GLASS includes a variety of clusters with different morphologies. The correlation between the properties of the Hα emitters and the hosting structure is the subject of Paper VIII, where we investigate trends with the clustercentric distance, the hot gas density as traced by the X-ray emission, the surface mass density as inferred from gravitational lens models, and the galaxy local density, in order to investigate in detail the role of the cluster environment in shutting down star formation.

We thank the anonymous referee for constructive and helpful comments. Support for GLASS (*HST*-GO-13459) was provided by NASA through a grant from the Space Telescope Science Institute, which is operated by the Association of Universities for Research in Astronomy, Inc., under NASA contract NAS 5-26555. We are very grateful to the staff of the Space Telescope for their assistance in planning, scheduling, and executing the observations. B.V. acknowledges the support from an Australian Research Council Discovery Early Career Researcher Award (PD0028506). T.M. acknowledges support from a Japanese Ministry of Education, Culture, Sports, Science, and Technology Grant-in-Aid for Scientific Research (26-3871), and from a Japan Society for the Promotion of Science research fellowship for young scientists.

Software: 3D-*HST* (Brammer et al. 2012; Momcheva et al. 2015), GiG (Schmidt et al. 2014; Treu et al. 2015).

APPENDIX A
GALAXIES SHOWING SIGNS OF RAM-PRESSURE STRIPPING

In this Appendix we show all the galaxies that, upon visual inspection, were classified as probable ram-pressure stripping candidates, both in clusters (Figure 19) and in the field (Figure 20), and that were not shown in the main text.

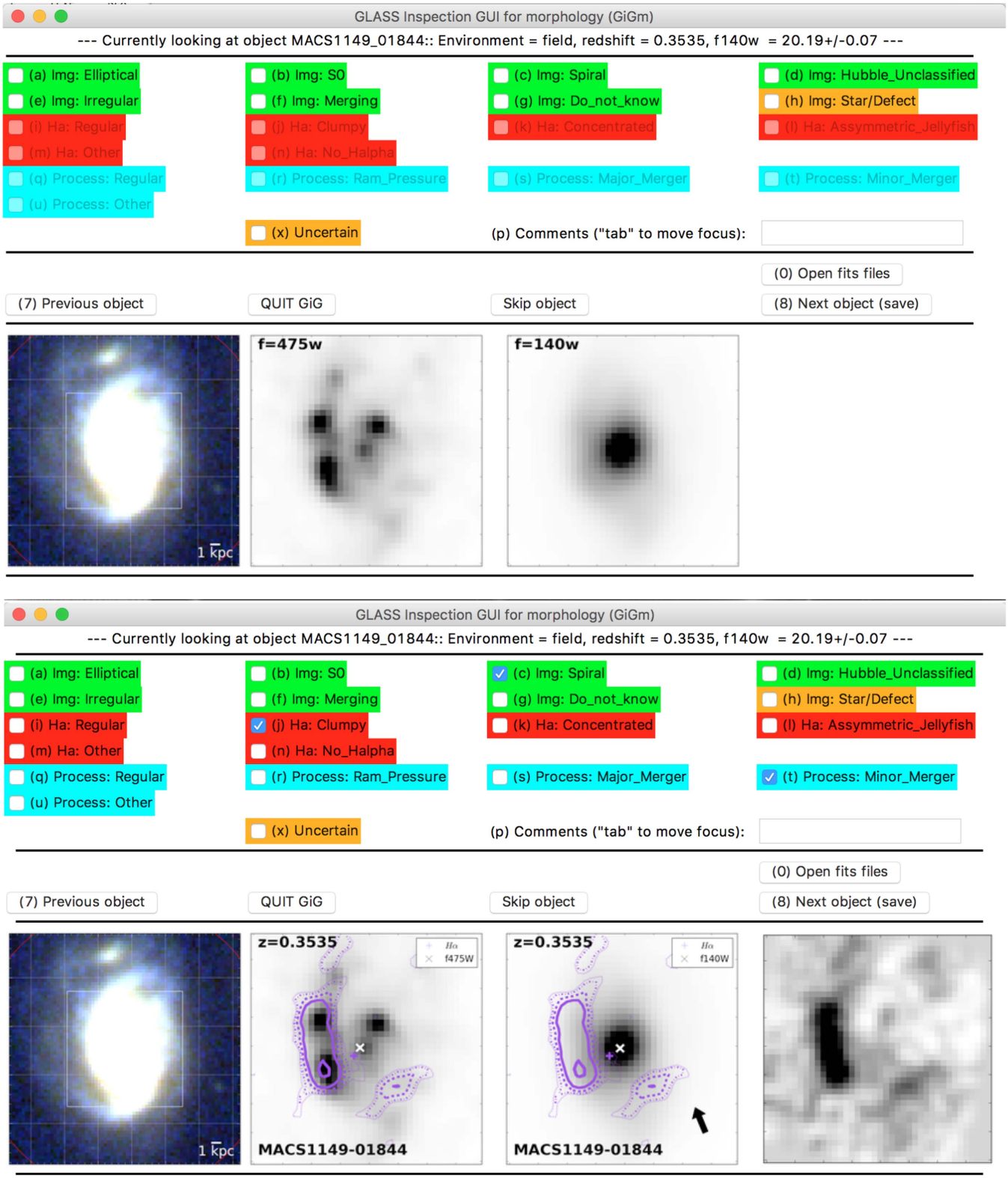

Figure 21. Overview of the GiGm interface for the clumpy Hα emitter MACS1149_01844 shown in Figure 12. The top panel shows the initial inspection window, which is used for all galaxies (Hα emitters as well as non-Hα emitters) classifying the morphology from direct image broad band postage stamps (green check-boxes). A color composite and images in F475W and F140W are shown here. If available, the .fits files of these can be opened with the "Open fits files" button to be able to manually adjust the scale and stretch of the images. If the direct images of an Hα emitter are inspected, after completing the morphological classification the Hα morphology (red check-boxes) and star formation process (cyan check-boxes) classification become active, and the Hα map postage stamp is shown and Hα contours are overlayed on the direct image postage stamps and the Hα map is shown as illustrated in the bottom panel. If the direct image morphology inspection is performed on an object from the non-Hα control sample, GiGm simply advances to the next object. This ensures truly independent inspections of the broad band morphology and the Hα morphology. GiGm is publicly available at https://github.com/kasperschmidt/GLASSinspectionGUIs.

APPENDIX B
THE GLASS INSPECTION GUI FOR MORPHOLOGIES (GIGM)

As described in the main text the GLASS inspection GUI for morphologies (GiGm) was developed to visually inspect the broad band continuum morphology from ancillary imaging of the cluster and field galaxies in both the Hα sample and the non-Hα sample. Similar to GiG and GiGz presented in the Appendix of Treu et al. (2015), GiGm is a `Python`-based software available for download at https://github.com/kasperschmidt/GLASSinspectionGUIs. GiGm is included in the most recent version of the self-contained script `visualinspection.py+` that also contains GiG and GiGz. This means that an already functioning installation of GiG and GiGz is trivially extended to also include GiGm by updating `visualinspection.py+`. In this Appendix we describe the basics of GiGm, but a more detailed description can be found in theGiG_README available at https://github.com/kasperschmidt/GLASSinspectionGUIs. An archival version of this software has been placed in Zenodo (Schmidt 2016).

GiGm is run on a separate data directory containing prepared .png (and .fits) images, Hα .png (and .fits) maps, and versions of the .png postage stamps with Hα contours overlayed. If the .fits images are located these can be opened with DS9 from within GiGm. A general overview of the interface of GiGm is shown in Figure 21. The top panel depicts the inspection of the broad band continuum morphology of the objects in the Hα and non-Hα control sample. After completion of this inspection the GiGm interface will be added the Hα map and Hα contours on the broad band images for Hα emitters as shown in the bottom panel of Figure 21. For non-emitters, GiGm will skip this step and simply advance to the next object in the data directory (or list of objects provided) when the broad band morphological classification is completed. This ensures that the inspections of the broad band morphology and the Hα morphology are truly independent. GiGm determines whether or not to enable the Hα inspection based on the files available, i.e., if an Hα map is present for the current object, the Hα classification will be enabled. The details of the options for the morphological and Hα inspections seen in Figure 21 are described in Section 3.6. To display the object information seen at the top of the GiGm windows in Figure 21, an information file is provided containing the object id, cluster name, redshift, magnitude, magnitude error, the name of the band the magnitude was measured in, and the environment (field or cluster) for each individual galaxy. The output of the visual inspections with GiGm is an `ascii` file where 1 indicates that a check-box was set and 0 marks a check-box that was not set. As noted in Section 3.6 we combined these outputs and adopted the most common classification for each object among the four independent inspections. In case of broad disagreement, the galaxies were re-inspected and discussed to reach agreement.

REFERENCES

Abramson, L. E., Gladders, M. D., Dressler, A., et al. 2016, arXiv:1604.00016
Abramson, L. E., Kelson, D. D., Dressler, A., et al. 2014, ApJL, 785, L36
Atek, H., Malkan, M., McCarthy, P., et al. 2010, ApJ, 723, 104
Balogh, M. L., Navarro, J. F., & Morris, S. L. 2000, ApJ, 540, 113
Bekki, K. 1999, ApJL, 510, L15
Bekki, K. 2009, MNRAS, 399, 2221
Bekki, K., & Couch, W. J. 2003, ApJL, 596, L13
Bertin, E., & Arnouts, S. 1996, A&AS, 117, 393
Brammer, G. B., Pirzkal, N., McCullough, P. R., & MacKenty, J. W. 2014, STScI Instrument Science Report WFC3 2014-03
Brammer, G. B., van Dokkum, P. G., Franx, M., et al. 2012, ApJS, 200, 13
Bretherton, Moss, James, et al. 2013, A&A, 533, A67
Brüggen, M., & De Lucia, G. 2008, MNRAS, 383, 1336
Bruzual, G., & Charlot, S. 2003, MNRAS, 344, 1000
Butcher, H., & Oemler, A., Jr. 1984, ApJ, 285, 426
Calzetti, D., Armus, L., Bohlin, R. C., et al. 2000, ApJ, 533, 682
Castellano, M., Sommariva, V., Fontana, A., et al. 2014, A&A, 566, A19
Chabrier, G. 2003, PASP, 115, 763
Cheung, E., Faber, S. M., Koo, D. C., et al. 2012, ApJ, 760, 131
Coppin, K. E. K., Geach, J. E., Webb, T. M. A., et al. 2012, ApJL, 749, L43
Darvish, B., Mobasher, B., Sobral, D., et al. 2016, ApJ, 825, 113
Darvish, B., Sobral, D., Mobasher, B., et al. 2014, ApJ, 796, 51
Domínguez, A., Siana, B., Henry, A. L., et al. 2013, ApJ, 763, 145
Dressler, A. 1980, ApJ, 236, 351
Dressler, A., Oemler, A., Jr., Couch, W. J., et al. 1997, ApJ, 490, 577
Dutton, A. A., van den Bosch, F. C., & Dekel, A. 2010, MNRAS, 405, 1690
Ebeling, H., Ma, C.-J., & Barrett, E. 2014, ApJS, 211, 21
Ellis, R. S., Smail, I., Dressler, A., et al. 1997, ApJ, 483, 582
Fang, J. J., Faber, S. M., Koo, D. C., & Dekel, A. 2013, ApJ, 776, 63
Font, A. S., Bower, R. G., McCarthy, I. G., et al. 2008, MNRAS, 389, 1619
Fossati, M., Fumagalli, M., Boselli, A., et al. 2016, MNRAS, 455, 2028
Fumagalli, M., Fossati, M., Hau, G. K. T., et al. 2014, MNRAS, 445, 4335
Garn, T., & Best, P. N. 2010, MNRAS, 409, 421
Garn, T., Sobral, D., Best, P. N., et al. 2010, MNRAS, 402, 2017
Gehrels, N. 1986, ApJ, 303, 336
Gómez, P. L., Nichol, R. C., Miller, C. J., et al. 2003, ApJ, 584, 210
Gonçalves, T. S., Basu-Zych, A., Overzier, R., et al. 2010, ApJ, 724, 1373
Goto, T., Yamauchi, C., Fujita, Y., et al. 2003, MNRAS, 346, 601
Graham, A. W., & Driver, S. P. 2005, PASA, 22, 118
Grogin, N. A., Kocevski, D. D., Faber, S., et al. 2011, ApJS, 197, 35
Grützbauch, R., Chuter, R. W., Conselice, C. J., et al. 2011, MNRAS, 412, 2361
Gunn, J. E., & Gott, J. R., III 1972, ApJ, 176, 1
Haines, C. P., Pereira, M. J., Smith, G. P., et al. 2013, ApJ, 775, 126
Hopkins, P. F., Kereš, D., Oñorbe, J., et al. 2014, MNRAS, 445, 581
James, P. A., Shane, N. S., Knapen, J. H., Etherton, J., & Percival, S. M. 2005, A&A, 429, 851
Kauffmann, G., White, S. D. M., Heckman, T. M., et al. 2004, MNRAS, 353, 713
Kaviraj, S. 2014, MNRAS, 440, 2944
Kelson, D. D. 2014, arXiv:1406.5191
Kennicutt, R. C. 1998, ApJ, 498, 541
Kennicutt, R. C., Tamblyn, P., & Congdon, C. E. 1994, ApJ, 435, 22
Kodama, T., Smail, I., Nakata, F., Okamura, S., & Bower, R. G. 2001, ApJL, 562, L9
Koekemoer, A. M., Faber, S., Ferguson, H., et al. 2011, ApJS, 197, 36
Koyama, Y., Kodama, T., Tadaki, K.-i., et al. 2013, MNRAS, 428, 1551
Kriek, M., van Dokkum, P. G., Labbé, I., et al. 2009, ApJ, 700, 221
Kroupa, P. 2001, MNRAS, 322, 231
Lang, P., Wuyts, S., Somerville, R. S., et al. 2014, ApJ, 788, 11
Larson, R. B., Tinsley, B. M., & Caldwell, C. N. 1980, ApJ, 237, 692
Lewis, I., Balogh, M., De Propris, R., et al. 2002, MNRAS, 334, 673
Lilly, S. J., & Carollo, C. M. 2016, arXiv:1604.06459
Livermore, R. C., Jones, T., Richard, J., et al. 2012, MNRAS, 427, 688
Lotz, J. M., Koekemoer, A., Coe, D., et al. 2016, arXiv:1605.06567
Madau, P., Pozzetti, L., & Dickinson, M. 1998, ApJ, 498, 106
Mantz, A., Allen, S. W., Ebeling, H., Rapetti, D., & Drlica-Wagner, A. 2010, MNRAS, 406, 1773
Martig, M., Bournaud, F., Teyssier, R., & Dekel, A. 2009, ApJ, 707, 250
McGee, S. L., Bower, R. G., & Balogh, M. L. 2014, MNRAS, 442, L105
Meert, A., Vikram, V., & Bernardi, M. 2015, MNRAS, 446, 3943
Menanteau, F., Ford, H. C., Martel, A. R. & ACS Science Team 2005a, BAAS, 37, 1228
Menanteau, F., Martel, A. R., Tozzi, P., et al. 2005b, ApJ, 620, 697
Merluzzi, P., Busarello, G., Dopita, M. A., et al. 2013, MNRAS, 429, 1747
Merluzzi, P., Busarello, G., Dopita, M. A., et al. 2016, MNRAS, 460, 3345
Mihos, J. C., & Hernquist, L. 1996, ApJ, 464, 641
Momcheva, I. G., Brammer, G. B., van Dokkum, P. G., et al. 2016, ApJS, 225, 27
Moore, B., Katz, N., Lake, G., Dressler, A., & Oemler, A. 1996, Natur, 379, 613
Moran, S. M., Ellis, R. S., Treu, T., et al. 2005, ApJ, 634, 977
Morishita, T., Abramson, L. E., Treu, T., et al. 2016, arXiv:1607.00384

Muzzin, A., Wilson, G., Yee, H. K. C., et al. 2012, ApJ, 746, 188
Nelson, E. J., van Dokkum, P. G., Brammer, G., et al. 2012, ApJL, 747, L28
Nelson, E. J., van Dokkum, P. G., Förster Schreiber, N. M., et al. 2016, ApJ, 828, 27
Nelson, E. J., van Dokkum, P. G., Momcheva, I., et al. 2013, ApJL, 763, L16
Noeske, K. G., Weiner, B. J., Faber, S. M., et al. 2007, ApJL, 660, L43
Omand, C. M. B., Balogh, M. L., & Poggianti, B. M. 2014, MNRAS, 440, 843
Paccagnella, A., Vulcani, B., Poggianti, B. M., et al. 2016, ApJL, 816, L25
Patel, S. G., Holden, B. P., Kelson, D. D., Illingworth, G. D., & Franx, M. 2009, ApJL, 705, L67
Peng, C. Y., Ho, L. C., Impey, C. D., & Rix, H.-W. 2002, AJ, 124, 266
Poggianti, B. M., Fasano, G., Bettoni, D., et al. 2009, ApJL, 697, L137
Poggianti, B. M., Fasano, G., Omizzolo, A., et al. 2016, AJ, 151, 78
Poggianti, B. M., Smail, I., Dressler, A., et al. 1999, ApJ, 518, 576
Porter, S. C., & Raychaudhury, S. 2007, MNRAS, 375, 1409
Porter, S. C., Raychaudhury, S., Pimbblet, K. A., & Drinkwater, M. J. 2008, MNRAS, 388, 1152
Postman, M., Coe, D., Benítez, N., et al. 2012, ApJS, 199, 25
Postman, M., Franx, M., Cross, N. J. G., et al. 2005, ApJ, 623, 721
Price, S. H., Kriek, M., Brammer, G. B., et al. 2014, ApJ, 788, 86
Quilis, V., Bower, R. G., & Balogh, M. L. 2001, MNRAS, 328, 1091
Schawinski, K., Lintott, C., Thomas, D., et al. 2009, MNRAS, 396, 818
Schmidt, K. 2016, kasperschmidt/GLASSinspectionGUIs: GLASS inspection GUIs, v3.0, Zenodo, doi: 10.5281/zenodo.161686
Schmidt, K. B., Rix, H.-W., da Cunha, E., et al. 2013, MNRAS, 432, 285
Schmidt, K. B., Treu, T., Brammer, G. B., et al. 2014, ApJL, 782, L36
Sobral, D., Best, P. N., Matsuda, Y., et al. 2012, MNRAS, 420, 1926
Sobral, D., Best, P. N., Smail, I., et al. 2011, MNRAS, 411, 675
Sobral, D., Stroe, A., Dawson, W. A., et al. 2015, MNRAS, 450, 630
Sobral, D., Swinbank, A. M., Stott, J. P., et al. 2013, ApJ, 779, 139
Stott, J. P., Swinbank, A. M., Johnson, H. L., et al. 2016, MNRAS, 457, 1888
Straughn, A. N., Kuntschner, H., Kümmel, M., et al. 2011, AJ, 141, 14
Stroe, A., Sobral, D., Dawson, W., et al. 2015, MNRAS, 450, 646
Stroe, A., Sobral, D., Röttgering, H. J. A., & van Weeren, R. J. 2014, MNRAS, 438, 1377
Swinbank, A. M., Smail, I., Sobral, D., et al. 2012, ApJ, 760, 130
Treu, T., Ellis, R. S., Kneib, J.-P., et al. 2003, ApJ, 591, 53
Treu, T., Ellis, R. S., Liao, T. X., et al. 2005, ApJ, 633, 174
Treu, T., Schmidt, K. B., Brammer, G. B., et al. 2015, ApJ, 812, 114
van Dokkum, P. G., Brammer, G., Fumagalli, M., et al. 2011, ApJL, 743, L15
Vogelsberger, M., Genel, S., Springel, V., et al. 2014, MNRAS, 444, 1518
von der Linden, A., Wild, V., Kauffmann, G., White, S. D. M., & Weinmann, S. 2010, MNRAS, 404, 1231
Vulcani, B., Poggianti, B. M., Finn, R. A., et al. 2010, ApJL, 710, L1
Vulcani, B., Poggianti, B. M., Oemler, A., et al. 2013, A&A, 550, A58
Vulcani, B., Treu, T., Nipoti, C., et al. 2016, arXiv:1610.04615
Vulcani, B., Treu, T., Schmidt, K. B., et al. 2015, ApJ, 814, 161
Wang, X., Jones, T. A., Treu, T., et al. 2016, ApJ, submitted (arXiv:1610.07558)
Willett, K. W., Schawinski, K., Simmons, B. D., et al. 2015, MNRAS, 449, 820
Wisnioski, E., Förster Schreiber, N. M., Wuyts, S., et al. 2015, ApJ, 799, 209
Wuyts, S., Förster Schreiber, N. M., Genzel, R., et al. 2012, ApJ, 753, 114
Wuyts, S., Förster Schreiber, N. M., Nelson, E. J., et al. 2013, ApJ, 779, 135
Yagi, M., Gu, L., Koyama, Y., et al. 2015, AJ, 149, 36
Yang, Y., Flores, H., Hammer, F., et al. 2008, A&A, 477, 789